2019

Investigation of Flow Field Structures in a Rectangular Channel with a Pin Fin Array

Patrick Tran
University of Central Florida

INVESTIGATION OF FLOW FIELD STRUCTURES IN A RECTANGULAR CHANNEL WITH A PIN FIN ARRAY

by

PATRICK KENDALL TRAN
B.S.M.E. University of Central Florida, 2016
M.S.B.M.E University of Central Florida, 2018

A thesis submitted in partial fulfilment of the requirements
for the degree of Master of Science in Mechanical Engineering
in the Department of Mechanical and Aerospace Engineering
in the College of Engineering and Computer Science
at the University of Central Florida
Orlando, Florida

Summer Term
2019

Major Professor: Jayanta Kapat

ABSTRACT

Pin fin arrays are commonly found in heat exchangers, turbine blades, and electronic heat sinks. Fin arrays are extended surfaces that are used as turbulence promoters by inducing horseshoe vortex (HSV) and von Karman vortex (KV) structures. The horseshoe vortex are primarily studied in the leading edge of the blunt body, whereas the KV are formed in the trailing side. This study presents an experimental investigation of flow field structures and pressure loss on staggered pin fin array in the wake region, where KV are dominate. These flow structures increase the local levels turbulence and generate eddies that promote flow mixing, which in turn allows for higher levels of heat transfer. Improvement in heat transfer can increase the efficiency of the heat exchanger by reducing the thermal load and stress on the components which can extended product life. A study of the vortex shedding using a Particle Image Velocimetry (PIV) technique is used to measure flow field using a closed loop vertical water tunnel. A Time Resolved Particle Image Velocimetry (TR-PIV) study for both steady and unsteady flow structures in the fully developed region of a pin fin array at multiple wall normal cross sections are performed. The pin fin array consists of circular pin fins with 8 rows of 7.5 pins in rectangular channel with Reynolds number varying from 10,000 to 20,000. The Pin array is in a staggered configuration with stream wise (Y/D) spacing of 2.5 and span wise (X/D) spacing of 2.5, and height to pin diameter (H/D) of 2. A supplemental computation fluid dynamic (CFD) study is also for comparison with the PIV flow field. The goal of the present study is to determine the major vortex structures that found the flow at different Z/D, quantify parameters that numerical methods are unable to solve, and provide a base line for other parameters that can be used to improve the accuracy of numerical models. The novelty of this work is to provide data and characterize the near the viscous sub layer of Z/D =0.

ACKNOWLEDGMENTS

I would like to express by gratitude to the Center for Advance Turbo Machinery and Energy Research as well as the Siemens Energy Center. It has been the place of my academic growth and my second home. The University of Stuttgart for their joint effort. My academic neighbors Propulsion Energy Research Lab (PERL) and Samik's lab. My colleagues along the way: all of the graduates students, post docs, as well undergraduates students who have helped me along the way. My Advisors Dr. Jayanta Kapat and Dr. Erik Fernandez. Finally my family for their unwavering support.

TABLE OF CONTENTS

LIST OF FIGURES

LIST OF TABLES

CHAPTER 1: INTRODUCTION

As mankind develops into more mature nation states, the demand for energy is ever increasing to meet the demands of industrial complexes, transportation, and personal use of energy. The current use of energy in the United States is about 100 quadrillion BTU, and in-order to convert energy systems from one state to another, some form of turbomachinery is used. To stay financially competitive, manufactures of turbomachinery components must set targets of improved efficiency in each iteration of their product to meet both customer demand as well as local and global governmental environmental constraints. The need to produce power is a challenge since the demand of power is increasing as lesser developed countries get access to energy and as modern counties industrialize into a larger and more dense cities. The challenge is to produce power with low economic demands, clean or zero waste system, or renewable methods in order to meet both practical and environmental demands placed by governments. With the increase pressure from legalization from carbon taxes, large governmental entities are funding methods to better understand fundamental and innovated solutions to solve the energy problem. One such area is better understanding and optimization of engine components and cycles.

Gas turbines are used in industry due to their ability to produce a large amount of power for their given size. The goal of engineers is to either maximize the power of a given engine or maximize the thermal efficiency of the engine. For engines to achieve higher efficiency or power production, combustion temperatures must reach higher temperature values for the ideal Carnot cycle efficiency shown in equation 1.1. However, the gas turbine follows the Brayton cycle and uses the Turbine inlet Temperature (TIT) as the maximum temperature. The Brayton cycle shown in Figure 1.1 shows a PV and TS diagram and is comprised of four main engine sections: the intake, compressor, energy source, and exhaust [1]. Reaching the hottest temperatures are ideal, however, there is an upper limit of temperature for conventional materials before catastrophic failure can occur. Thus, begins the drive for aggressive cooling mechanisms to lower thermal load on engine

components.

$$\eta = 1 - \frac{T_{Inlet}}{T_{Turbine}} \tag{1.1}$$

The main parameter driving the thermal efficiency in turbines is the pressure ratio, since increasing the pressure ratio increases the turbine inlet temperatures. However, increasing the inlet temperature too much can lead to engine failure if not controlled within the limits of the material. To prevent engine failure due to temperature load on engine components, engineers design complex cooling schemes that move compressed air into areas where cooling of components is required. This extra step, however, provides no useful work unless a larger gain in efficiency is found elsewhere. Sometimes, a gain in thermal efficiency is outweighed by the price of coolant flow. Teams of engineers design and analyze difference cooling mechanisms to provide the most cooling while minimizing the the amount of compressed air needed. A combination of power and thermodynamic efficiency will be used as a crude direction which engineers tend to design for. There are three directions normally engineer try to work for as an engineering goal in their process map, the first being the increase the efficiency with the same given work, the other is to produce more work at the same given efficiency, and finally the reduction of cost in the machine. Depending on the application, the target of thermal efficiency or power is determined. More efficient engines tend to be slower, which might not be able to keep up large gradients in engine speed, such as a jet aircraft when a large range of power range might be needed during various stages of lift off, cruise speed, and landing. In either case, higher TIT is a goal since it provide a means to produce both.

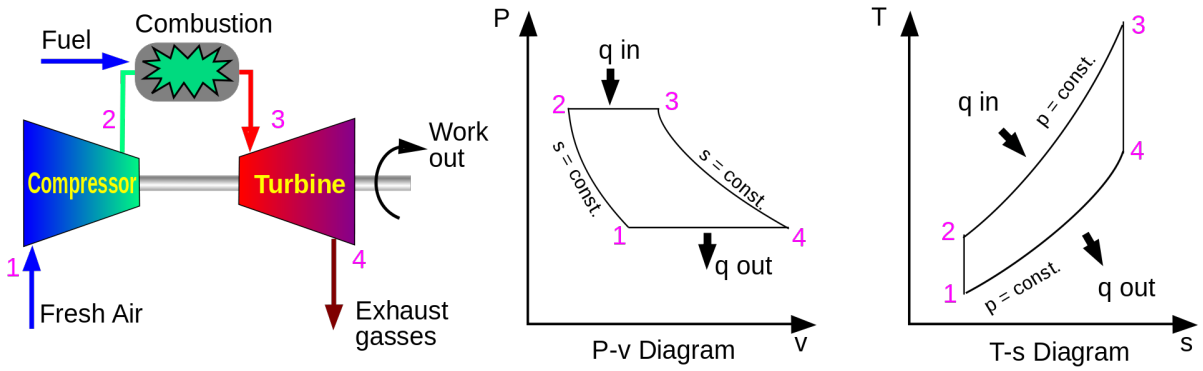

Figure 1.1: Sketch of Jet Engine Components and Thermodynamics States [1]

As seen in the Carnot equation, another path to increase efficiency is to place the engine in colder ambient temperatures. However, environmental conditions are not always consistence and mother nature has control over atmospheric conditions and the geography of the region. Therefore, the only other logical choice is to improve the combustion temperature. The chosen fuel source will be the upper possible limit in the cycle calculations found in equation 1.1. For land-based gas turbines, natural gas is commonly used by power production companies because of its cost and availability. For aero-based engines, kerosene is the most common due to energy density for weight considerations. Other engines are also designed for fuel flexibility, or hybrid fuel sources. Methane has a flame temperature of 1950 C while Kerosene has a flame temperature of 2100 C. Both temperatures are well past the melting temperature of Inconel (1400 C), one of the most exotic alloys available with modern technology. Therefore engineers are interested in protecting components through the means of coolant.

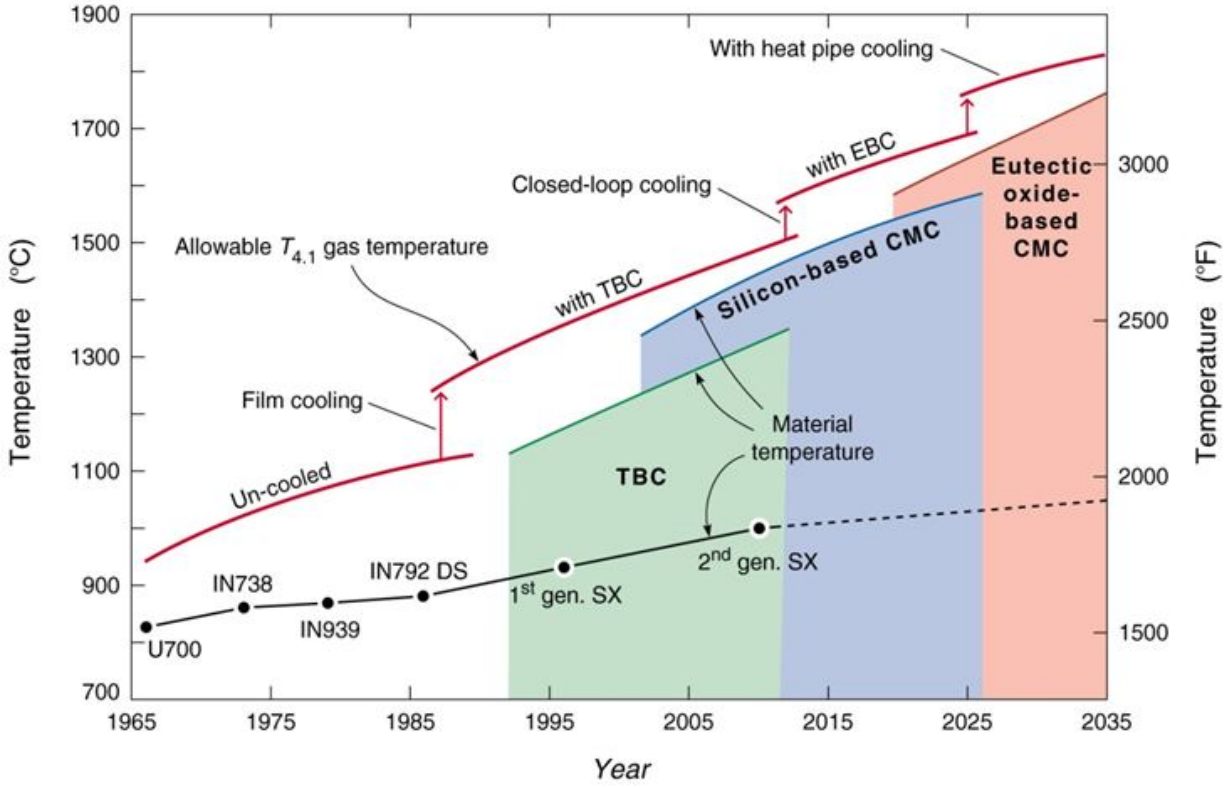

Figure 1.2: Turbine Temperature Growth over Time [http://www.virginia.edu/ms/research/wadley/high-temp.html, 2015]

Engineers design gas turbines with very high temperature inlet conditions in order to achieve high power output as well as improve the thermal efficiency to meet the demands of industrial applications. However, increasing the temperatures also brings some devastating consequences. The current thermal load of most advance gas turbines well exceeds the melting temperatures of turbine blades and require many novel cooling techniques in order to operate. To reduce the thermal load, cooling schemes are introduced to ensure the engines can safely operate at high inlet temperatures by allowing the turbine blade surface to be sufficiently cooled. Some methods of

cooling consist of both internal cooling channels, transpiration cooling, as well as some methods of external cooling.

Four areas are primarily studied in order to increase the inlet temperatures, this is to improve the efficiency while keeping it within the material limits. They are external convective cooling, internal convective cooling, high resistance thermal barrier coating, and material of the actual turbine blade. Figure 1.3 shows a schematic which shows the three main sections that provide protection the the blade by the means of coolant via convective cooling. Film cooling sections are considered external cooling features, whereas the internal cooling passages and impingement cooling is provided by internal cooling. Both high heat transfer and lower heat transfer coefficient help aid the cooling of a turbine blade. Fluids can act as insulators or aid in thermal mixing which can both be an aspect to help maintain the temperature of the turbine blade. Convective cooling mechanisms are not limited to engines. Similar systems are found in heating, ventilation, and air conditions (HVAC) systems found in homes to keep in home temperature a comfortable temperature. Building structures are well insulated to keep sun's temperature away the home, like thermal barrier coatings found on the first few stages of the turbine section. Air conditioning systems have vents at strategic points in each of the rooms to maximize mixing to ensure the heat gets pumped out of the building via the heat pump. Normally not found in homes, but found in commercial buildings are air locks, which are successive doors within a short distance. Air locks are double layered doors with a room allows use air as a buffer region between outdoor temperature and the cool room temperature.

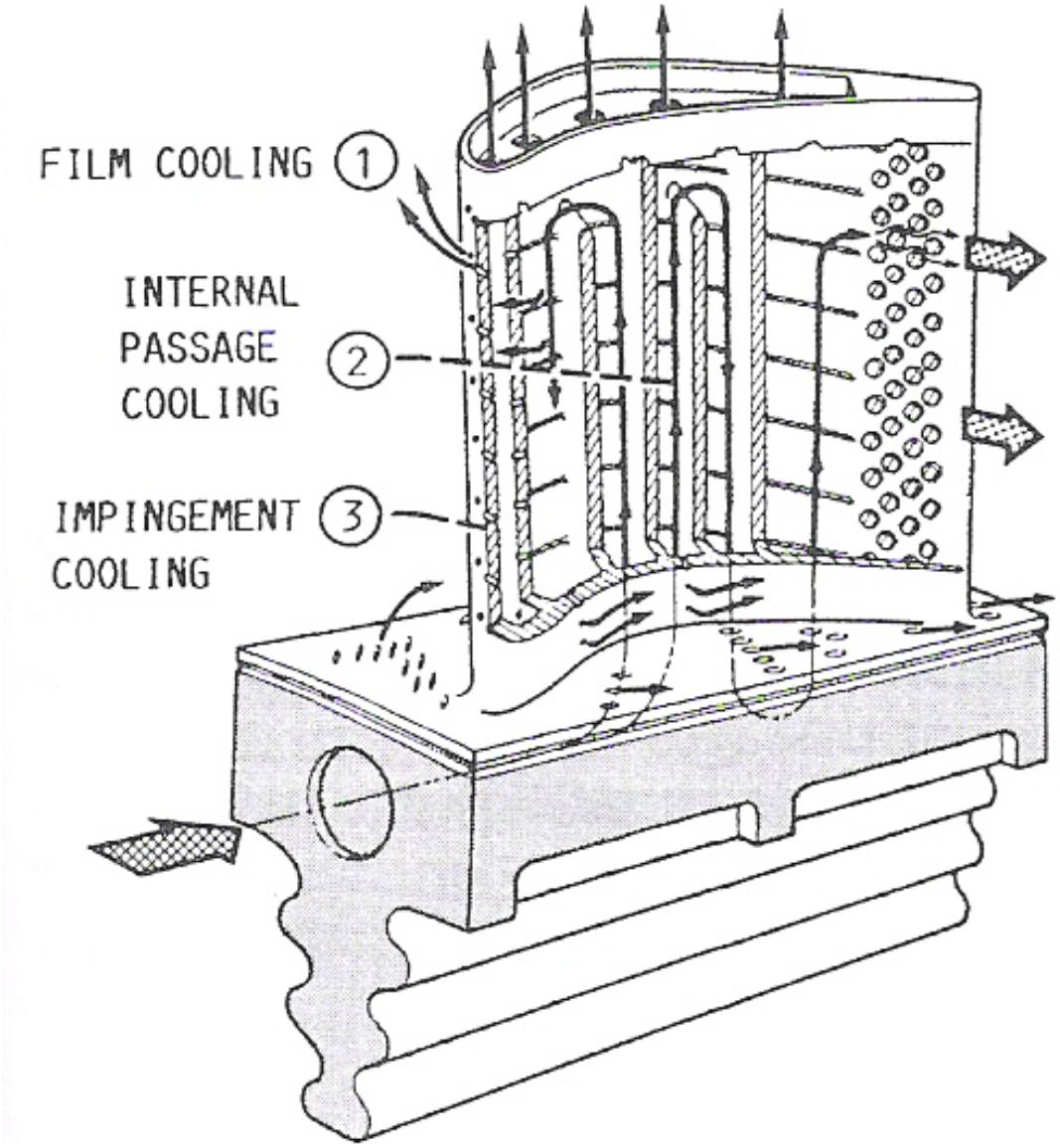

Figure 1.3: Turbine Blade showing various cooling mechanisms [2]

The focus of this paper will only be focused on the trailing edge of the turbine, which sees improved heat transfer by pin fin arrays. This field of study is considered internal cooling passages. Figure 1.4 shows two main core flow features that are studied, it is well known that the following features influence the level of heat transfer in pin-fin arrays:

- Surface Area (Wetted Area)
- Reynolds number
- Horseshoe vortex
- Vortex shedding
- Turbulence
- Multi Dimensional effects

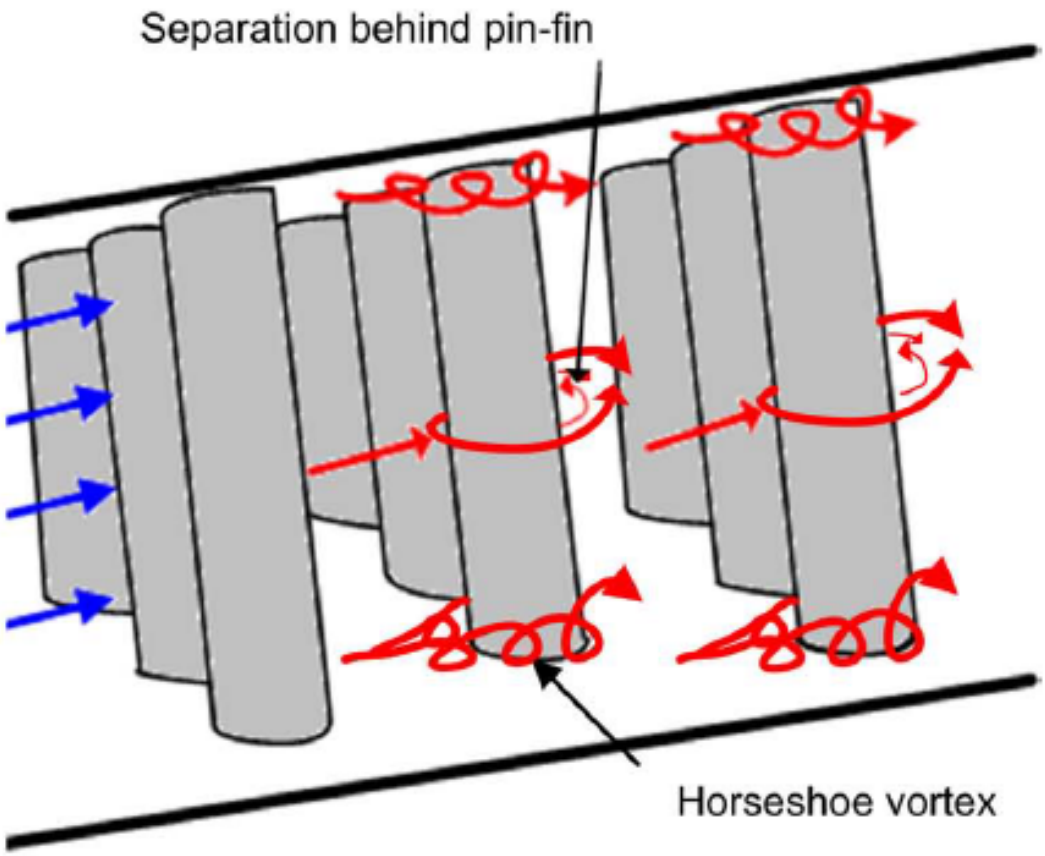

Figure 1.4: Flow field Features Found in Pin Fin Arrays [3]

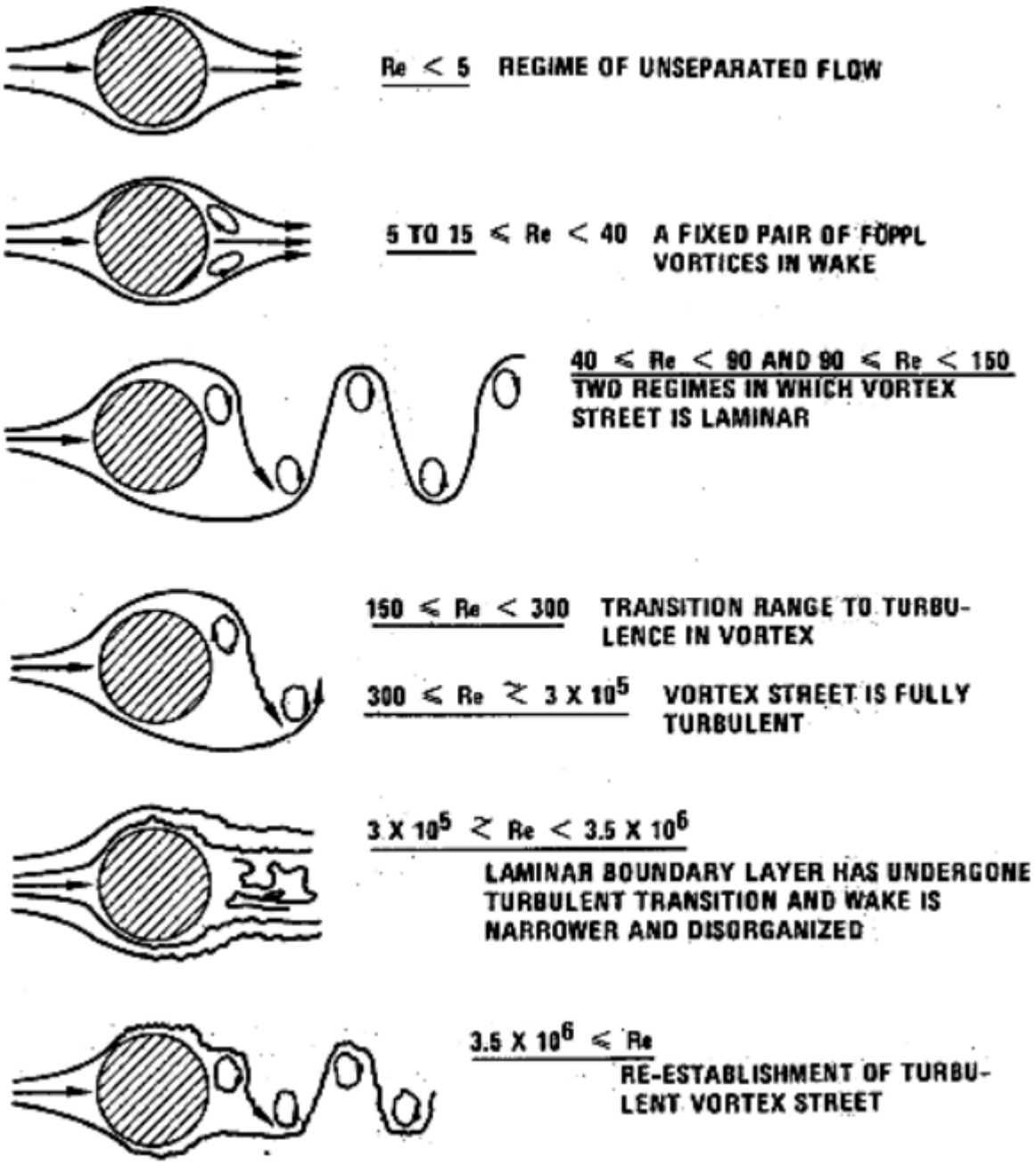

Figure 1.5: Wake Formation around pin based on Reynolds Number [4]

Pin fins can be used as a cooling aid in other areas beside turbine blades. Figure 1.5 shows that other than turbine cooling, computer cooling components is another market in which they are used. Heat sinks and heat exchanges for air conditioning units use nearly identical features as well as radiator systems. Figure 1.6 shows a cross section of a turbine blade, showing the current area of study.

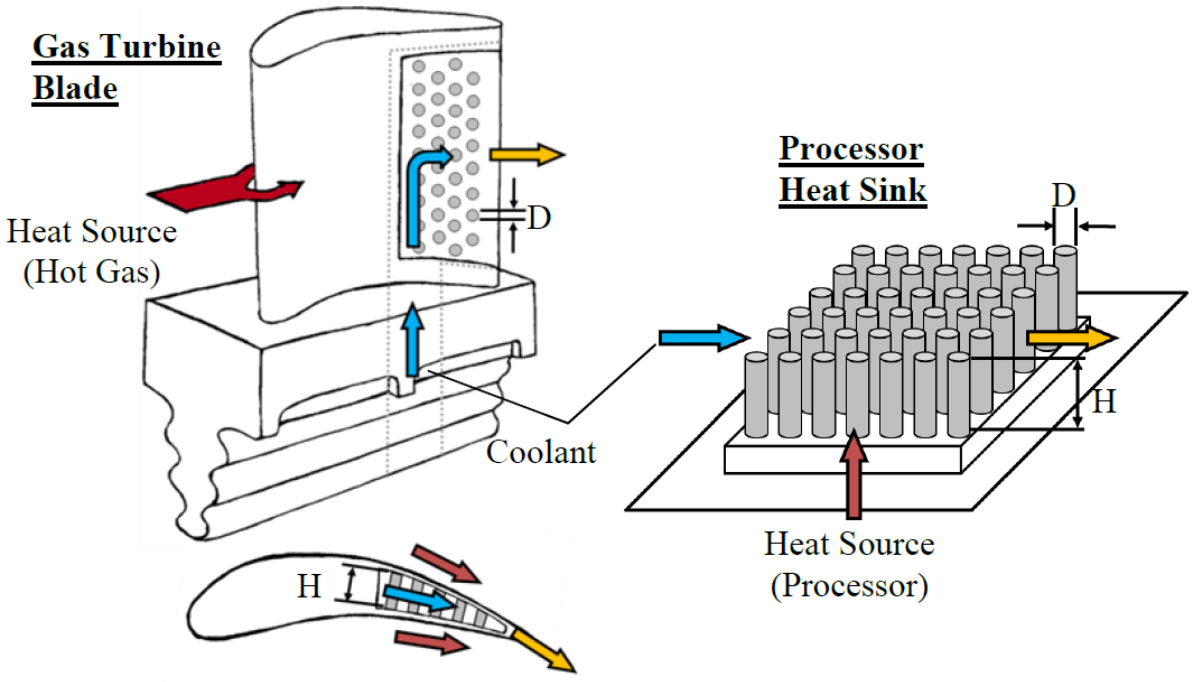

Figure 1.6: Common uses of Pin Fin Arrays Used as Heat Transfer Promoters [3]

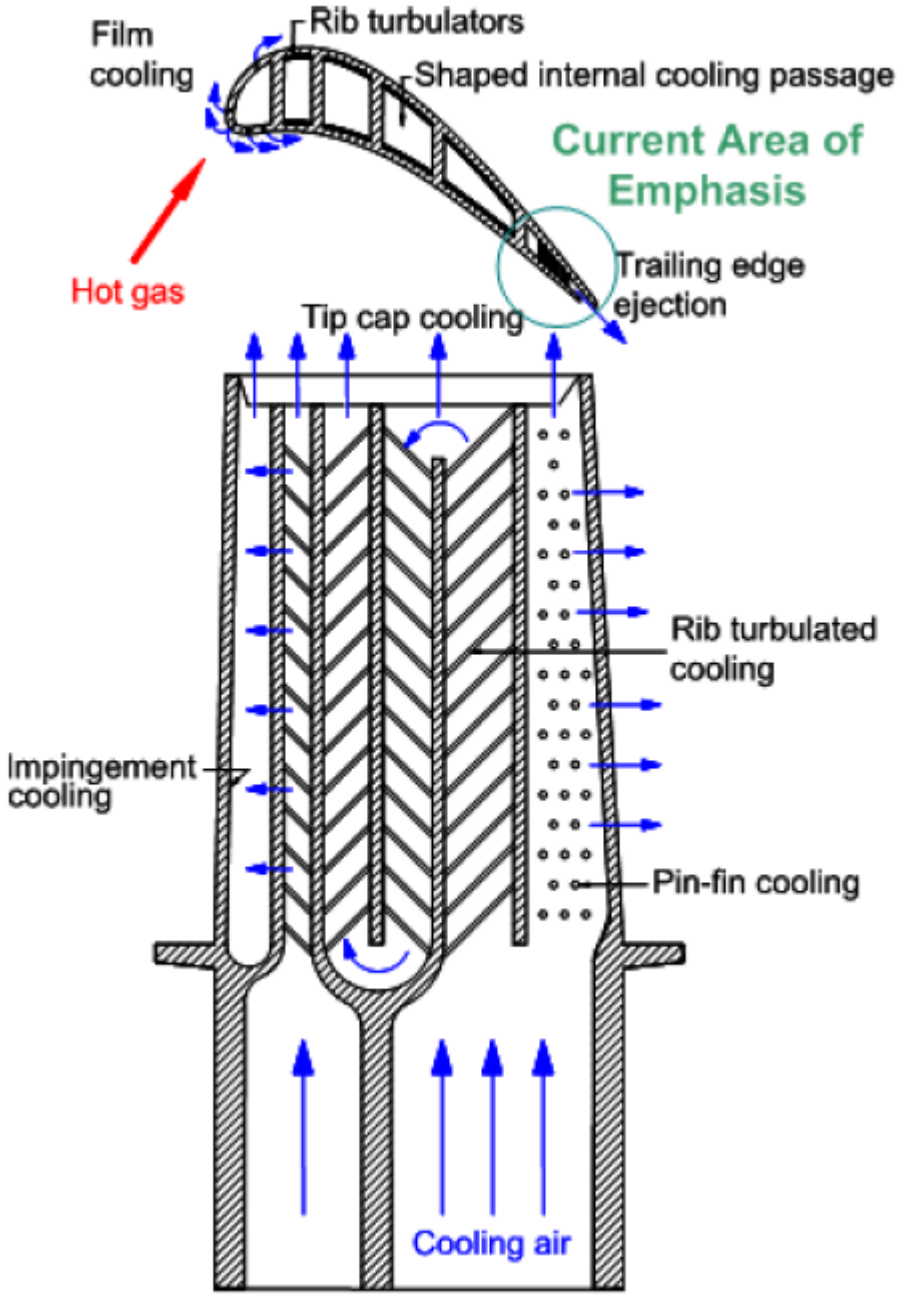

Figure 1.7: Area of Interest of Trailing Edge [3]

CHAPTER 2: LITERATURE REVIEW

Internal cooling channels primarily consist of the leading edge cooling, serpentine pass channels, followed by the trailing edge. Serpentine passages rely on turbulence promoters and various parameters such as type, size, and angles and a majority of these parameters is studied by Han et al. [2, 5], as well as other groups such as Berger and Hau [6], Bailey and Bunker [7] and Wang et al. [8] study many internal flow geometries. This paper will focus of the trailing edge aspect, and will investigate the flow structures in a staggered pin fin array. Zukauskas first popularized pin Fins in the late 1960 with large height to diameter ratios [9]. Baker studied the horseshoe formation on a single wall bound cylinder with the help of smoke and oil flow visualization [10]. Since then, many other parameters have been looked, such as different pin geometries, spacing, and Reynolds number on the heat transfer effectiveness. Heat transfer effectiveness is most commonly studied by copper block techniques or various local heat transfer measurement techniques [11, 12, 13]. However, there are a limited number of studies for a pin fin array that are fully spatially resolved for flow field. Most if not all flow structure studies have been performed by Metzger [14], Ames [15], Bianchini [16], and Van Fossen [11]. Metzger reports heat transfer and friction factor correlations for short pin fin arrays for Reynolds numbers up to 50,000 using Hotwire. Ames developed a correlation to predict the local heat transfer based on Reynolds, turbulence, diameter, and length scale using Hotwire While the use of PIV in study Pin Fin array have been performed by Uzol [17] and Ostanek [18] in Pin Fins before, however, are limited to single pin fins, or single row of pin fins, or entrance effects of turning angle.

Internal cooling in gas turbines is another subset of fluid mechanics compared to external flows. For heat transfer enhancement, generally the exposed surface area of the structure is increased, therefore changes the nature of the bulk flow. Large changes in geometric constraints, such as adding rib turbulators drastically change the flow, while dimples generally does not influence the bulk flow as much. Drasitcally changing the bulk flow can cause large pressure gradients,

increasing the drag and increases the pressure loss in the system. For internal cooling, the channel diameter is not heavily studied, due to geometric constraint of the manufacturing as well as a technique of non- dimensional parameters used to help approximate change of scale renders this almost useless. Most of the research in internal flows deals with surface geometries adding into the flow channel, such as dimples, pin fins, ribs, and derivatives and combination of these designs to change the surface boundary conditions of the N-S equations. Han et al [2] studies parameters other than hydraulic diameter like the one seen for jet diameter, which is more important and defines an aspect of internal flows physics better than the hydraulic diameter by itself would. The aspect ratio for a rectangular channel is the channel height to length. However, Han et al also studies other parameters such as rib orientation, rib shape, and rib pitch-height ratio [5]. Like in the case of external geometries, creativity will eventually lead to a never ending cycle in this field. For now, only standard shapes are used because of ease of manufacturing, however, once complex shapes are well understood, there might be a way to maximize heat transfer augmentation with additive manufacturing.

Impingement cooling is a subset of internal cooling, however, is not classified as conventional internal duct cooling. There are two types of flows studied in open literature: single and array of impinging jets. This technique is not only used in gas turbine cooling, and can be found elsewhere, such as electronic cooling and HVAC systems. Since the effect of one jet heavily effects the neighboring jets, much of literature separates these two systems as single jet and multi jet arrays. Bunker studies all aspects of turbine cooling, where most academics only studies are limited to one section going into detail [19]. Pin Fins were first used by Zukauskas in the late 1960 with large height to diameter ratios [19]. This is known in the fin effect in conductive heat transfer, however, the external cooling mechanism is altered when a geometric object is introduced in the flow path. Since then these shapes have been considered by many other researchers, studying end wall heat transfer, stream wise and span wise spacing. Baker considered the horseshoe formation on a single wall bound cylinder with the help of smoke and oil flow visualization [10]. External

cooling is primarily film cooling is a technique devised in the 1960's which was is a form of convective cooling. Goldstein defines film cooling to be an introduction of a secondary fluid (non hot gas path) at one or more discrete location along an exposed high temperature surface [21]. The basis of convective cooling is to bleed air from cooling channels to form a protective film of cold air protecting the turbine blade from the hot gas in the combustion. There is a large field in studying fluid mechanics in this area from institutions all over the world. Over 2000 papers and publications have been written in this field since 1960's. The main parameters in film cooling are jet diameter, jet geometry, and jet length as well as combinations of the three. Boyce has many papers in investigating jet length leaving the film hole [22] while Kohli studies [23] varying Jet Lengths vs Jet Diamter, and Bunker has many studies on shaped holes [24]. Since flow structures are heavily based on geometric considerations, there will be a never ending research as it will always be open due to the lack of understanding the fluid mechanics of complex flows with the introduction of turbulence and open to creative of complex shapes. Not many detail flow measurements are currently found in literature with an unsteady flow measurement at various Z/D. The work present here is study primary flow features and their contribution vortex shedding, turbulence, and three dimensional flow field effects found in a staggered pin fin array.

CHAPTER 3: METHODOLOGY

Flow Diagram

The flow field measurement was investigated in a closed loop vertical water tunnel powered by a 7.5 hp Water pump, capable of moving 1400 liters of water per minute. The flow rate is controlled by a variable frequency drive which can be controlled increments of 0.6 Hz. The VFD controller allows for adjustments of speeds between 40 percent to 100 percent of max speed. The max speed is based on the electrical frequency supplied which is 3 phase 400V 60 Hz. The pump is powered by a 60 Hz 3 phase signal in the United States, resulting in the 0.6 step size of frequency. The flow diagram is shown in figure 3.1. At the start of the test, all valves are closed with the outside reservoir filled to its max capacity. Valve 1 is then opened, allowing water into the piping into the inlet of the pump. The vent on the pump is then opened allowing the pump to be primed. Valve 5 is then opened allowing water into the filter system. The vents on the filter systems are open until they are primed and all air is removed from the lines. Valve 6 is then opened to allow water into the upper tank. Up until this point, the hydro static pressure should naturally push the water in the piping system. The pump is then turned on until the necessary water for the test condition is obtained which is marked at a location on the sight glass on the tank. The location marked is the highest location of the perforated plates, which serves as a flow conditioner. Once the tank has been filled to the critical level, the pump is then turned off and valve 1 is then closed. Valve 3 is then opened, and time is passed to allow for the plumping to be vented. The pump is primed once more. Once the pump is primed, the pump is turned on to the necessary frequency for the desired flow rate. The filter system can run for to ensure the water quality is homogeneous and all debris has passed the filter system. It is suggested that the filter is run for at least 30 minutes. After the system has been filtered, the filter system is bypassed by opening valve 7 and closing valve 5. Seeding is added to the system via the upper tank. A buffer time of 30 minutes is taken

to allow the the flow system to reach homogeneous conditions with the particles before testing is begun. Addition Rig pictures can be found in APPENDIX A: RIG PICTURES.

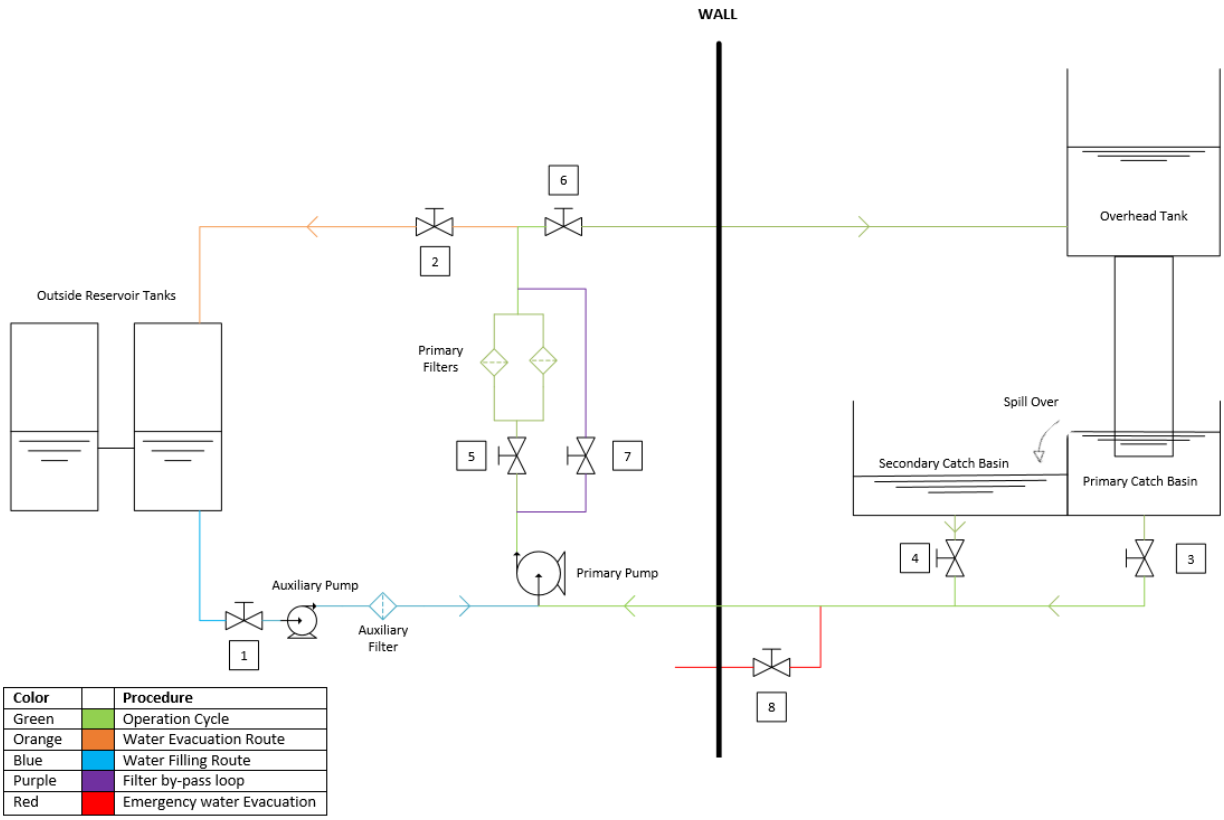

Figure 3.1: Flow Diagram of Test Setup

Test Section

The test section is made up of 8 rows of 7.5 staggered pin fins in rectangular channel made from 2.54 cm thick acrylic. The use of acrylic is for necessary for optical access for the laser sheet. Half pins are used at alternating ends to ensure the open area between the pins are constant per row. Each pin was machine from a solid circular rod made from PVC to a diameter of 39 mm and

with a height of 78 mm. The X/H spanwise spacing is 2.5 and the Y/H stream wise spacing is 2.5.

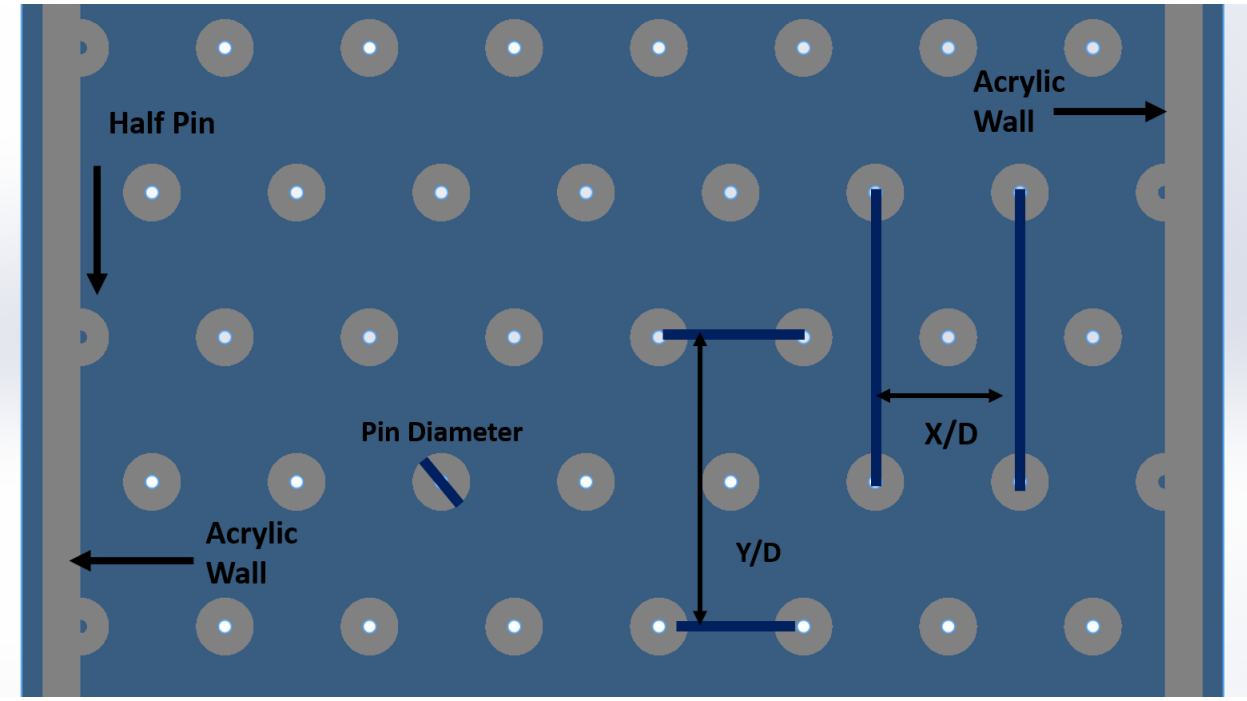

Figure 3.2: Geometric Spacing of Test Section

The area of interrogation is marked of the orange rectangle, between the 6th and 7th row found in Figure 3.2 Literature has found that pin fin arrays have reached fully developed conditions after the 4th row. The area of interest was selected to impose fully developed conditions in the CFD simulation for the inlet and modeling periodic conditions to reduce mesh size.

Reynolds number of the flow is calculated based on average velocity using the mass flow rate and minimum cross-section between the pin and the pin diameter. The velocity, although is an average is know to be Vmax in literature. Flow rates were measured from a venturi flow meter measured at the inlet of the the upper tank. The test section of the pin fin array consist of 8 rows of 7 and a half pins. The pins are in a staggered array allowing the open area to be consistent in each

row. The rectangular channel is made from 2.54 cm thick acrylic sheet on all four sides. The inlet contains a bell mouth and as well as a perforated plate that serves as flow conditioners, allowing for a smooth transition of the flow into the test section. There is also a developing section, which is approximately 15 diameters between the bell-mouth exit and the first row of pins. This ensures the flow rate is fully developed prior to reaching the pin fins.

The seeding particle was aluminum oxide which was 3 micro meter in diameter. The choice of seeding was chosen to satisfy stokes flow and drag equation shown by Equations 3.1 and 3.2 respectively. Stokes number was also calculated and is required to be less than unity for particle tracing techniques. Stokes law is applied such that the drag and Force of gravity and Force of gravity are unison. General Stokes drag assumes that following conditions:

- Spherical Particles
- Homogeneous (uniform in composition) material
- Smooth Surface
- Particles do not interfere with each other (no collision)

$$Stokesdrag = 6 * \pi * \eta * r * u \tag{3.1}$$

$$Fgravity = \frac{4}{3} * \pi * r^3 * (\rho_s - \rho_f) * g \tag{3.2}$$

Particle Image Velocitemetry

The PIV test campaign was performed via two methods: steady and unsteady. Both test have the same area of interrogation show in in Figure 3.2 The steady case resolves average statistics that can be seen within the test section, whereas the unsteady case consist of time resolved

data. Time resolved data is both temporal and spatially resolved, whereas average statistic is only spatially resolved. The first method was to obtain mean flow field at three cross sectional planes and was performed using a pulsed Quantel Evergreen 200mJ Nd:YAG laser. The laser beam was focused using a spherical lens, then split using cylindrical lens to obtain a light sheet. The steady vector fields were obtained at a rate of 15Hz, with 2420 image pairs using a pair of Andor Zyla 5.5 megapixel (2560x2160 pixel) CMOS camera fitted with a Scheimpflug adapters. Scheimpflug adapters are necessary to position cameras that are not perpendicular to the focal plane of interest when taking stero PIV measurements. It allows the focal plane to be rotated when the sensor is not parallel to the area of interest. The second method consist of using an Otoengine 1.5 Watt continuous wave laser from with PCO1200 high-speed camera capturing at 500 frames per second at full frame. Image pairs were post processed using a LaVision's DaVis 8 a commercial software using a robust method of cross correlation. Another software that was heavily used was MATLAB, which includes a package PIVLAB which also uses the same fundamental method from cross correlation, however, PIVLAB does not use LaVision's algorithms to find low intensity particles, optimizations techniques, or statistical analysis to reduce uncertainty.

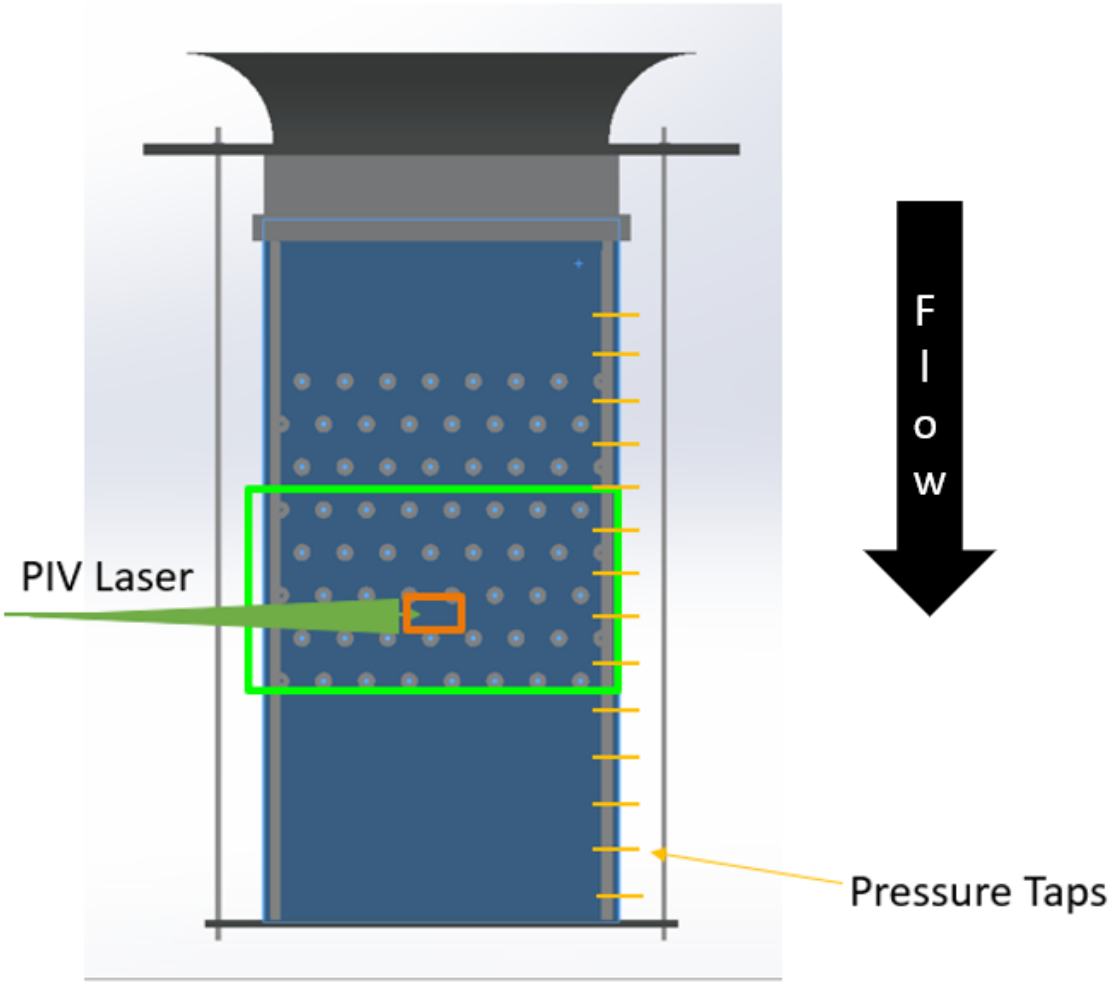

Figure 3.3: Cross Section of Water Tunnel

A high precision calibration plate was purchased from LaVision. Figure 3.3 shows a recorded image taken of the calibration grid. The plate is double sided with a dual plane capable of calibrating depth perception for stereo PIV and well as standard PIV. Only one plane is used to calibrate 2D PIV. LaVision's calibration plate claims to provide:

- High precision dot pattern
- Dot thickness tolerance less than +/-0.02mm
- Dot spacing tolerance of (largest separation on one side) down to +/- 0.02 mm

The calibration plate allows for determination of the scale factor and spacing which is used to convert the images into space coordinates.

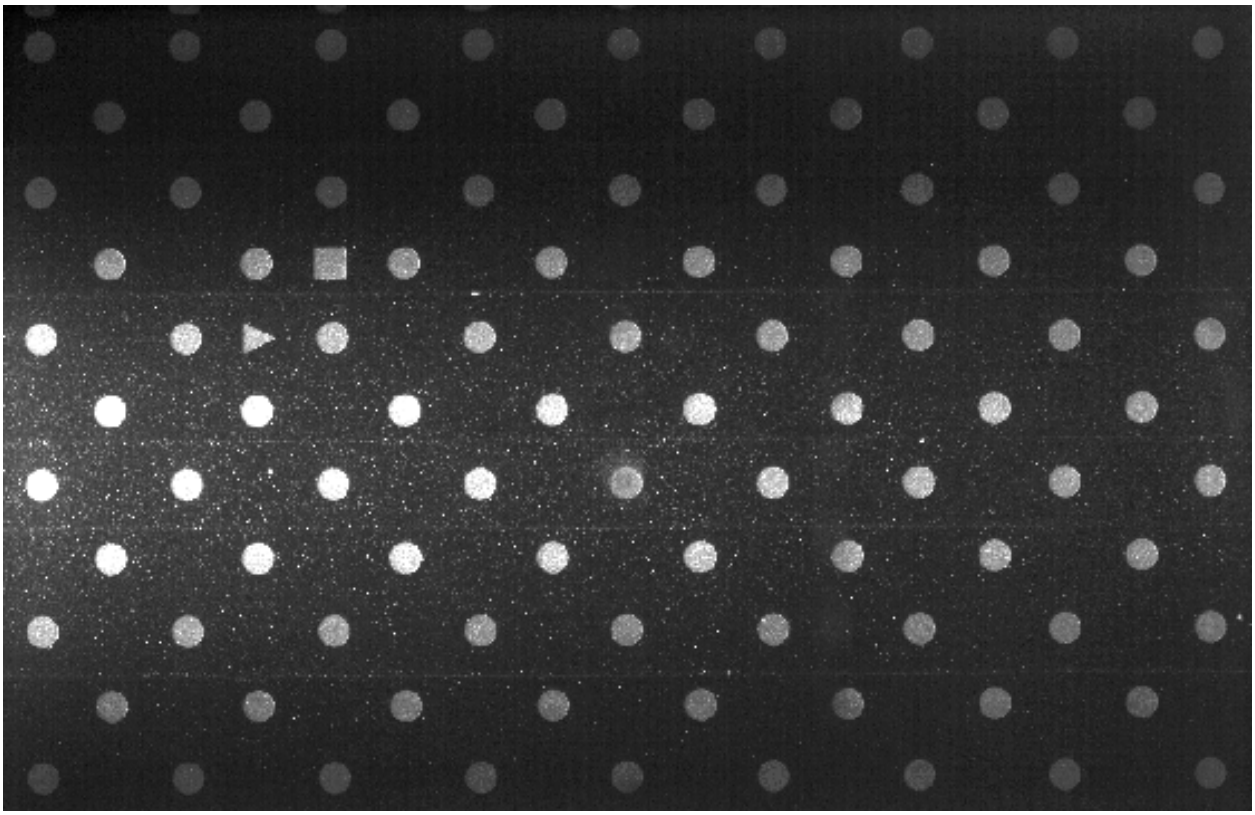

Figure 3.4: LaVision Calibration Plate used to Defined Pixel Displacement and Pixel Size

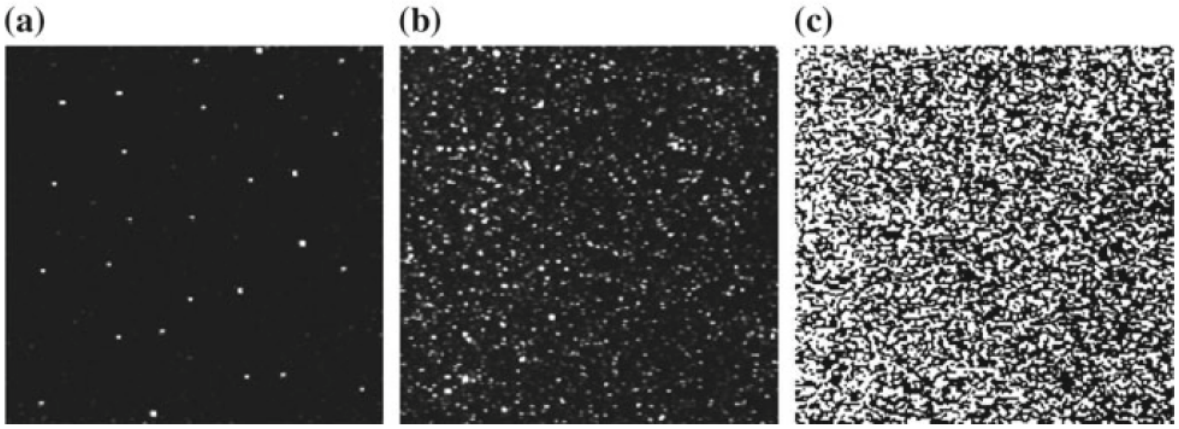

Figure 3.5: Ideal Particle Density in Interrogation Window [20]

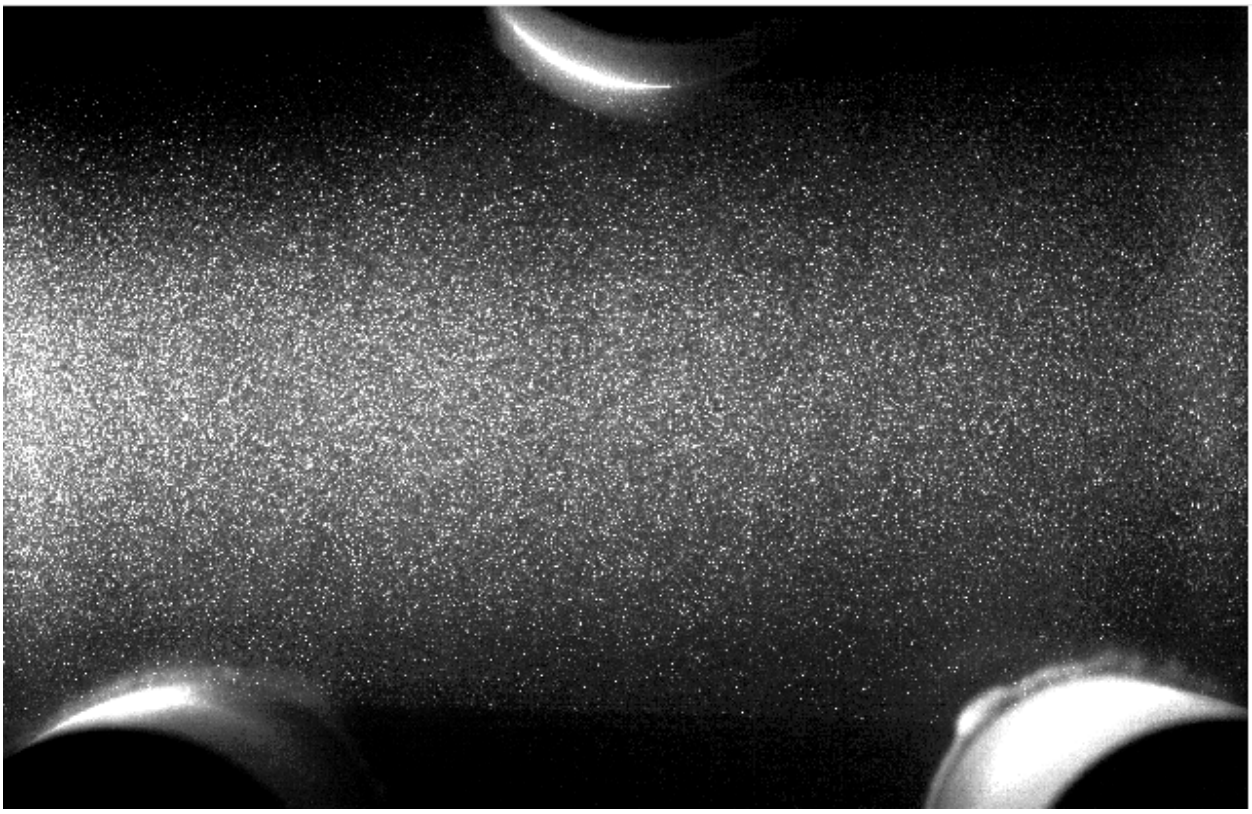

Figure 3.6: Image of Seeding Particles During Testing

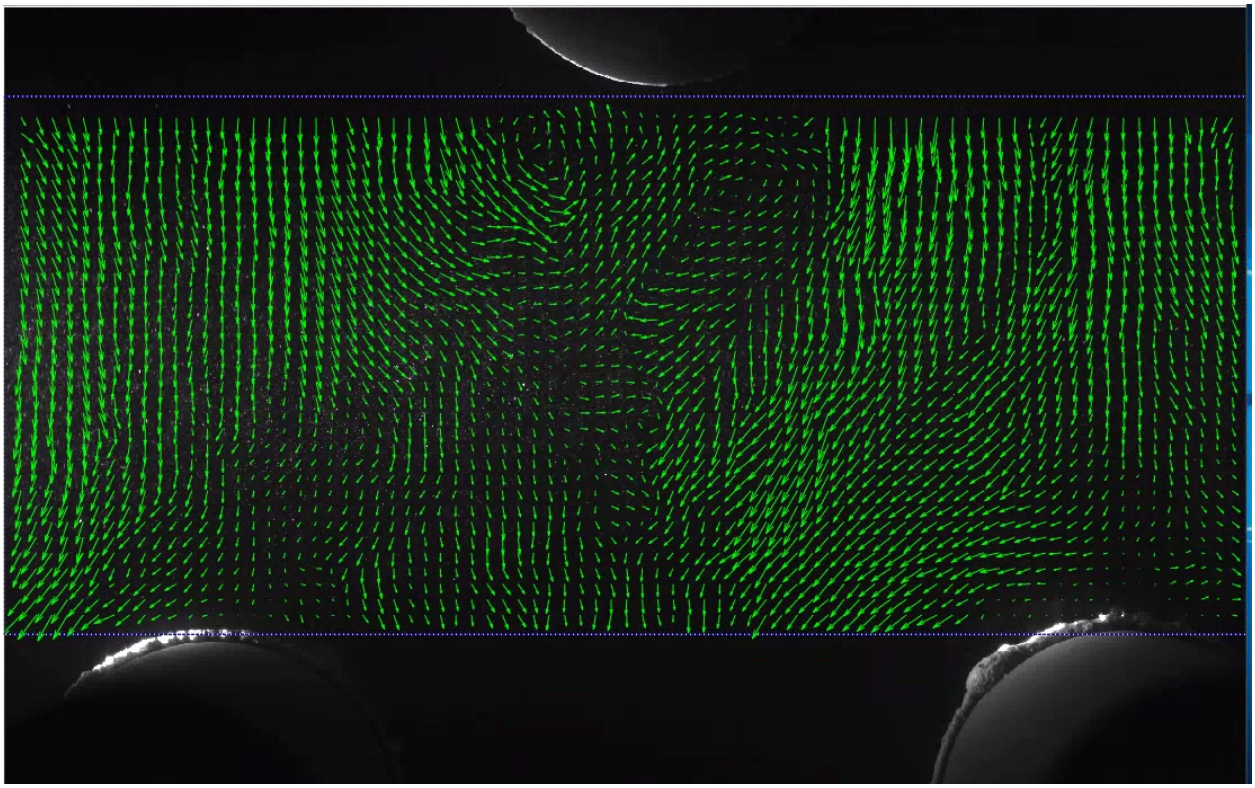

Figure 3.7: Instantaneous Velocity Field Mapped onto Particle Field

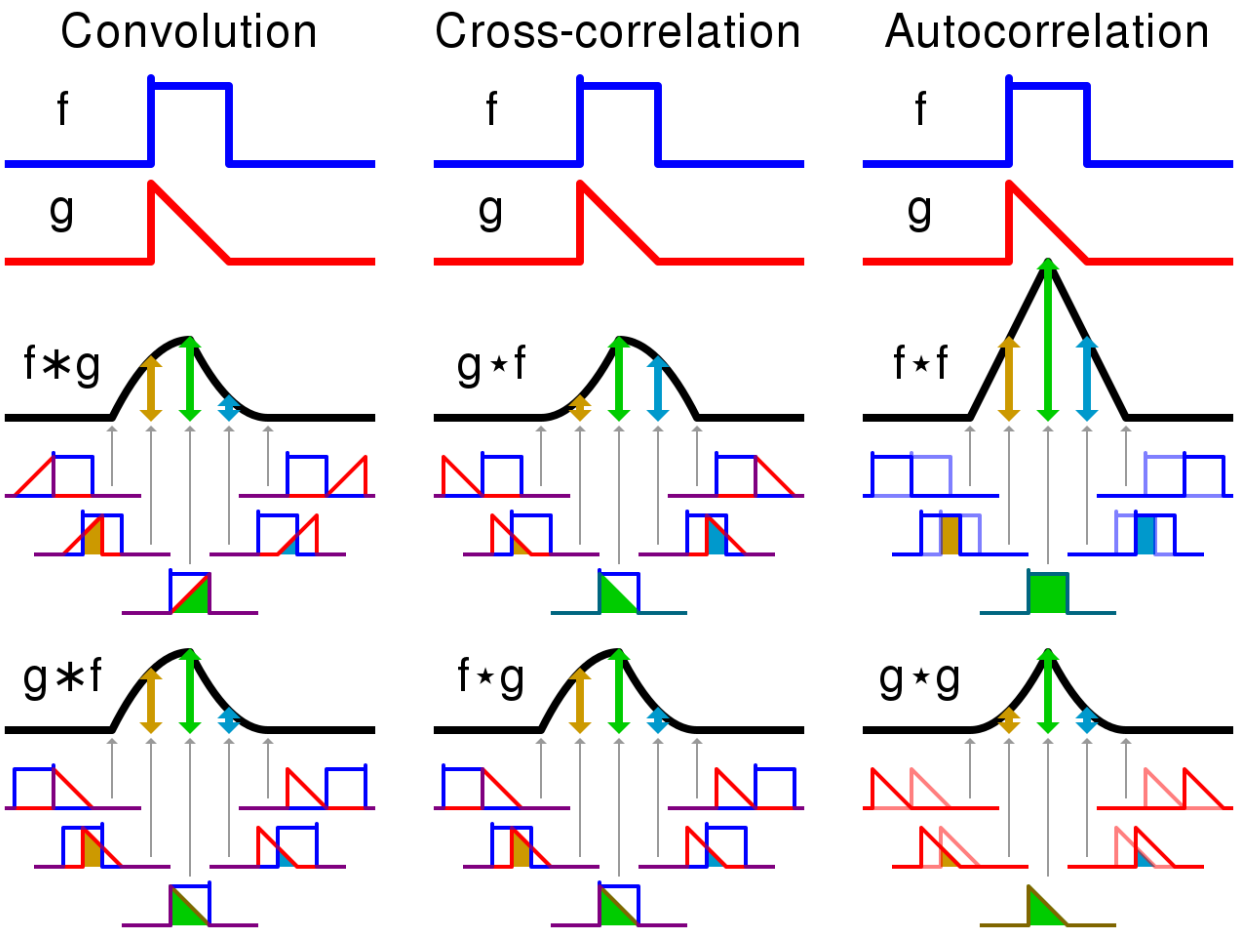

Figure 3.8: Visual on Mathematical Operations Used to Compare Two Signals

Using one of the correlations involves finding the intensity of the particle that is recorded from Image 1 and comparing it to another signal a small delta t later is recorded. When the dot product reaches a maximum, it is assumed that it is the same particle packet that in image 1. Binning pixel groups into interrogation windows instead of particles ensures groups of particles packets are found and the vector is correct. Figure 3.4 shows the ideal particle density that should be achieved, where Figure 3.5 shows the particle density achieved during testing. After processing

with PIVLAB, a vector field shown by Figure 3.6 can be calculated and be superimposed onto the original image. Various methods of correlations between the two signals used as a particle trace have been used shown in Figure 3.7. The method of cross correlation is also know to be very similar to the convolution operation, which is also known as a sliding dot product. During the post processing, a high interrogation window overlap scheme was used to achieve increased spatial resolution. Therefore, high particle image density was provided, on the order of 8 to 12 particles per 32 x 32 pixel interrogation window, with a pixel displacement on the order of 5 pixels per time step. Additionally, the universal outline detection scheme implemented within DaVis 8.3 was used to minimize the numbers of spurious vectors in the final resultant velocity fields. After vector correlation, an ensemble average of the velocity fields is performed to yield the statistical quantities of interest. Final vector resolution is 0.25 mm x 0.25 mm.

Table 3.1: Summary of dt and Vector Field Frame Rates

Reynolds Number	Frame Rate (Hz)	Exposure Time (micro second)
10000	320.91	1300
15000	472.64	1300
20000	618.58	1300

In addition to the experimental set up, a numerical study was performed. Star CCM+ version 14.02, a commercial software package for computational fluid dynamics (CFD) was used. The following simulations were performed using implicit unsteady Reynolds Average Navier Stokes (RANS) equations using a Shear Stress Transport k-Ω model. The model contains 1 pitch span-wise (1 * X/D) and 2 pitches stream wise (2 * Y/D). Fully Developed periodic boundary conditions were used for the inlet and outlet, as well in the stream wise wall. Line traces of various velocity was used as part of a mesh convergence study using mesh size of 3 million, 5million, 7 million,

and 9 million cells. The Mesh can be found in Figure 3.9. It was found that a 5 million cell mesh was enough for comparison with the experimental data. Shear Stress Transport k-Ω: The standard k-Ω model is capable of resolving flow through the boundary layer. SST k-Ω is a hybrid model that combines the k-Ω turbulence model and k-Ω turbulence model. This model ensures that the appropriate model is used in every part of the flow field (k-Ω in the wall region and the k-Ω away from the wall) [22]. First first grid size was chosen such that there were 15 prism layers and the base size of 1mm, this resulted in a mesh of about 3 million cells. The base size was decrease to reach and approximate grid change of 2 million cells per iteration.

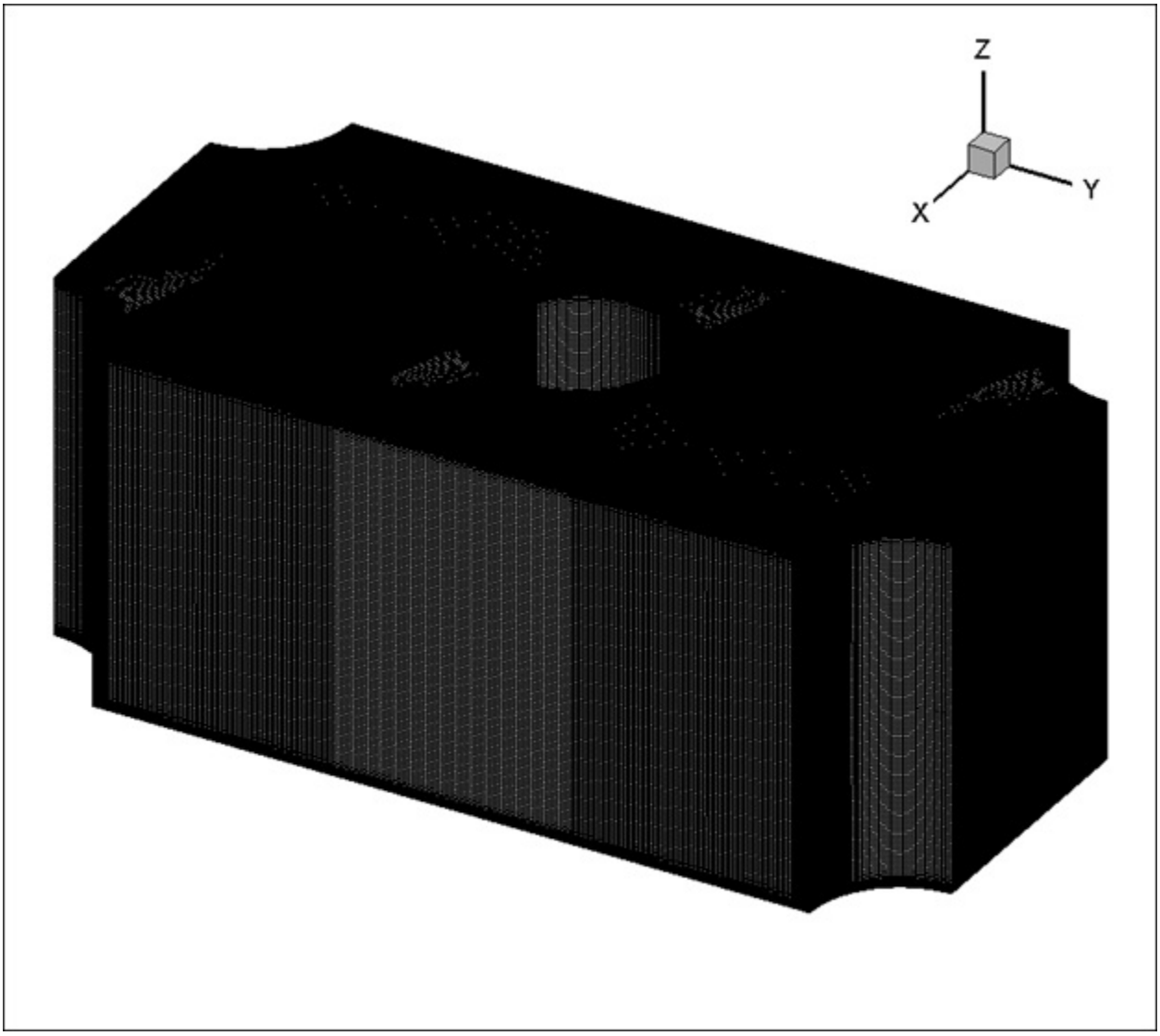

Figure 3.9: Mesh Grid Used in Star CCM

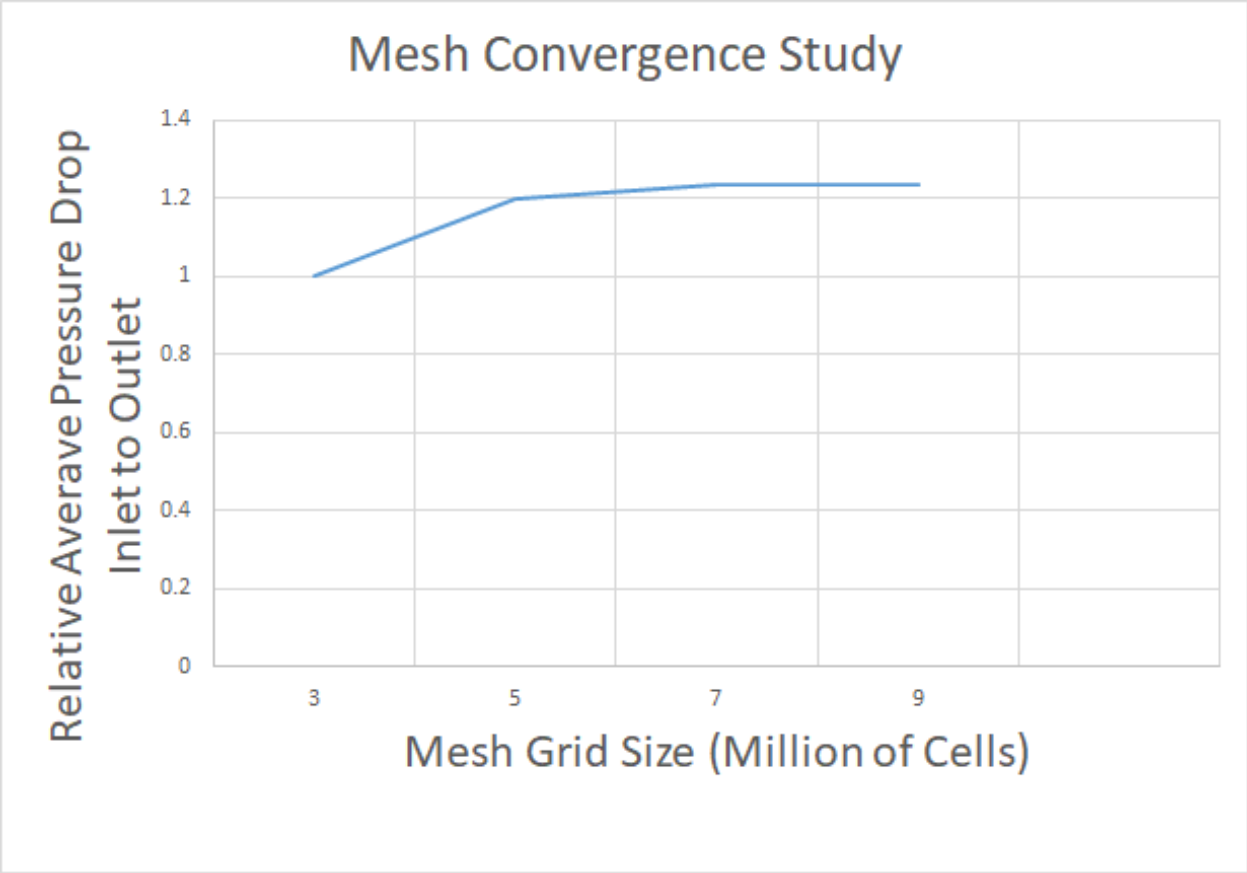

Figure 3.10: Convergence Study Based on Cell Count

Sources of Error and Uncertainty

No experiment is without error; however, it must be kept to a minimum. The pressure transducers that were used in the experiment were selected to achieve the maximum resolution for the expected pressure drop. The OMEGA wet/wet pressure transducer outputs an electrical current output between 0.4 mA and 20 mA and a resistor of 220 Ω was selected to achieve a voltage output between 0 and 5 Volts, making the best use number bits provided by the NI DAQ. The pressure transducer was calibrated against a micro pressure calibrator as well as a U tube manometer for

ranges outside of the calibrator. Experimental uncertainties have been estimated by the methods described in ASME PTC 19.1-2005, Kline and McClintock, and Moffat [27]. Error is based on a 95 % confidence level.

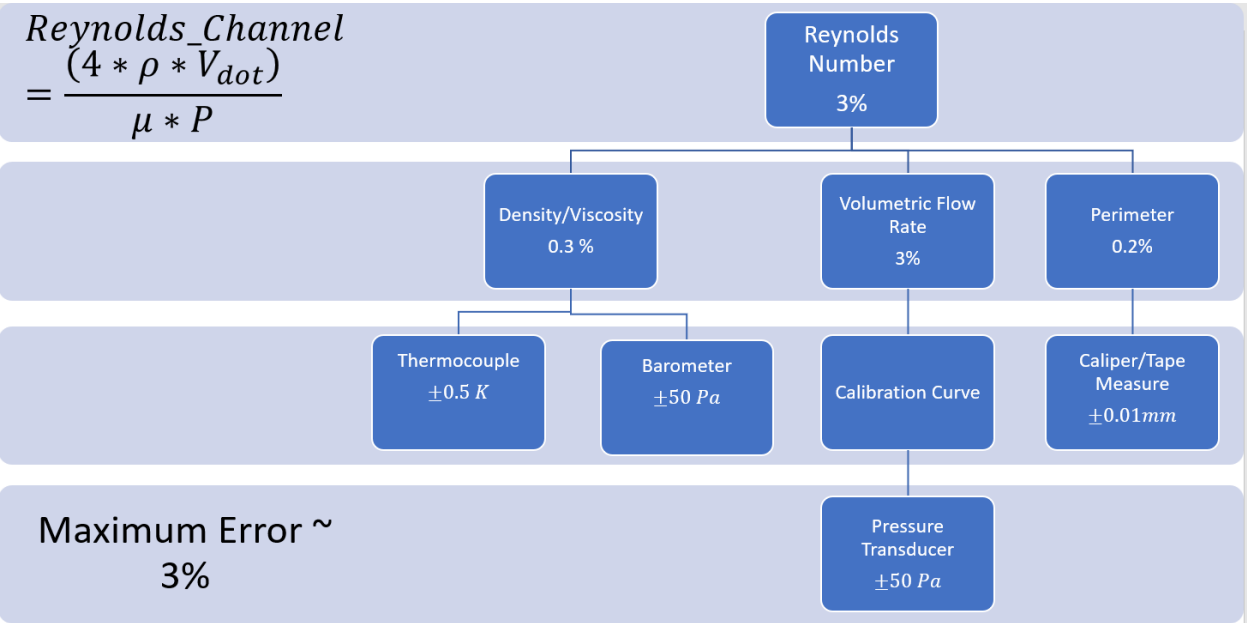

Figure 3.11: Uncertainty Tree for Reynolds Number Calculation

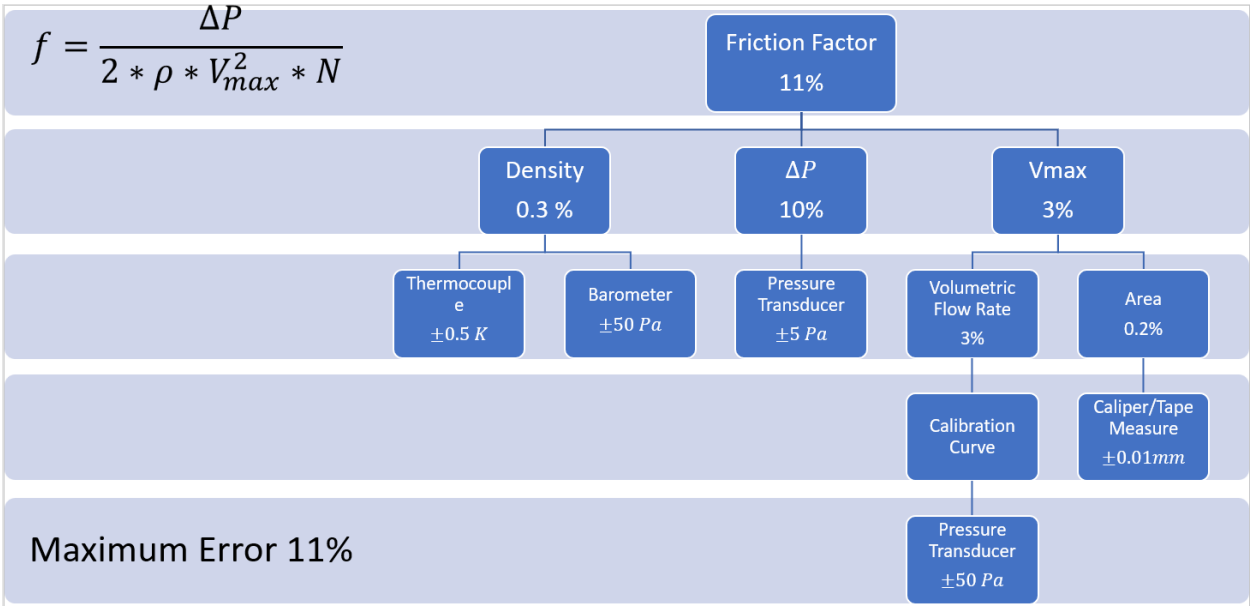

Figure 3.12: Uncertainty Tree for Friction Factor Calculation

After the experiment it was found that the laser sheet was off set on the order of 1mm from one corner of the test section to the other. The test section is approximately 750mm in the span-wise direction. This results in about a 0.001 degree error in the PIV interrogation plane measurement. It it is noted that one of the planes of interest is defined as Z/D=0, however by definition that is exactly at the end wall. It is the authors intention that Z/D = 0, represents the closest the author was able to get to the wall without any reflections, and results in a physical value that was approximately 1 mm from the wall, which should be Z/D = .025. This represent a 3 % error by using a normalized definition.

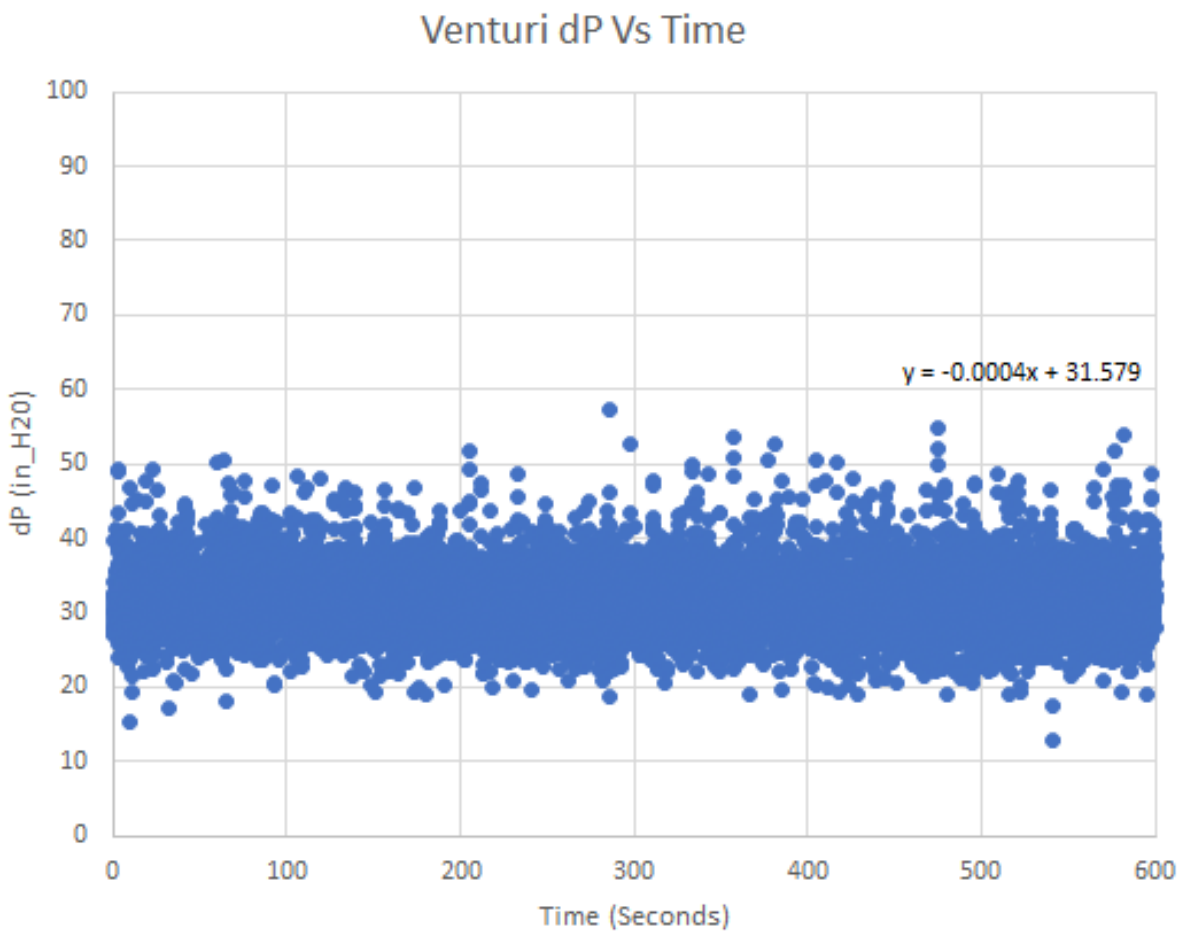

Figure 3.13: Plot of Venturi Reading vs Time

Flow measurements were taken for a period of 30 minutes to ensure steady state had been achieved, however, final reported measurements of flow rate takes an average of 1 min of pressure data read from the venturi. It was found that taking an average between these two time periods resulted in a less than 4 Liter per min of flow rate error. The total flow rate in the channel is on the order of 1000 liters per min, which gives rise error of less than .5 % once the system has reached

steady state. APPENDIX B: MATLAB CODE contains a code generated to plot the flow rate.

Bias and precision is then calculated using a 95% confidence interval using the students t score table assuming that all systematic errors could be kept to a minimum. Figure 3.10 and 3.11 show an uncertainty tree for the Reynolds Number and Friction Factor with their respective error. The worst case uncertainty has been shown.

The uncertainties of the vector components of Velocity in the X, Y, and Z obtained by the PIV were calculated using LaVision DaVis 8.3 software. This software uses the Wieneke's correlation statistics method [20] to calculate the uncertainties. In this method, the two images are overlapped on each other by the computed displacement vector field. In an error free measurement, these paired images exactly match which does not happen in real experiments. The particle image size, seeding density, displacements, shear, etc. influence the accuracy of the experiment. Using the statistical analysis of the disparity between the two images the uncertainty of a displacement vector is estimated.

Uncertainty in the time resolved Stereo-PIV results were estimated utilizing the technique described by Wieneke [20], in which the computed displacement field is used to compare correlated interrogation windows in the first and second image-pair frames. Differences in these frames are related to correlation functions, and are then used to calculate the random uncertainty of displacement vectors. These resulting uncertainties are both spatially and temporally resolved.

CHAPTER 4: FINDINGS

Validation

Friction test was performed with fourteen equally spaced pressure taps on the sidewall measured by an Omega water pressure transducer. There are pressure taps installed on the side wall at the same pitch as the pins but instrumented half way in-between each pin row. The pressure transducer output an electrical signal that was collected by a 16bit NI USB-6215 DAQ via MATLAB. Static Pressure was sampled at 20 Hz for 1 minute, for 1200 samples. Simultaneously the flow rate is measured by a similar pressure transducer, which is then used to calculate Reynolds Number with properties based on the ambient pressure and temperature of the water as well as Vmax. Hydro static pressure was also accounted for in the pressure drop of the rig, a separate test prior to the test was performed to measure those values, with the exception that the flow was in a static condition. That is, water was in the test section with the exit valve is closed and no there was no dynamic movement of the water. The hydro static pressure is subtracted from the respective static port during the dynamic run. This is subtracted from the pressure measurement read. Equation 4.1 shows the equation that was used to calculate friction factor.

$$f = \frac{\Delta P * Dh}{\Delta x(\frac{1}{2} * \rho * Vmax^2)} \tag{4.1}$$

Curve fitting data with a method of least squares with a power function found from literature leads to the equations found by Equations 4.2, 4.3, and 4.4.

$$f_{MetzgetHigh} = 1.76 * Re^{-0.318} \tag{4.2}$$

$$f_{MetzgetLow} = 0.317 * Re^{-0.132} \tag{4.3}$$

$$f_{Ames} = 0.5462 * Re^{-0.1912} \tag{4.4}$$

Table 4.1: Friction Factor Validation

Re	UCF	Metzger Low	Metzget High	AMES	Percent Difference (UCF and AMES)
9000	0.0997	0.0952	0.097	0.0957	% 4.2
15000	0.0909	0.0893	0.0831	0.0872	% 4.2
20000	0.0837	0.0859	0.0758	0.0825	% 1.5
24000	0.0784	0.084	0.0717	0.0797	% -1.6

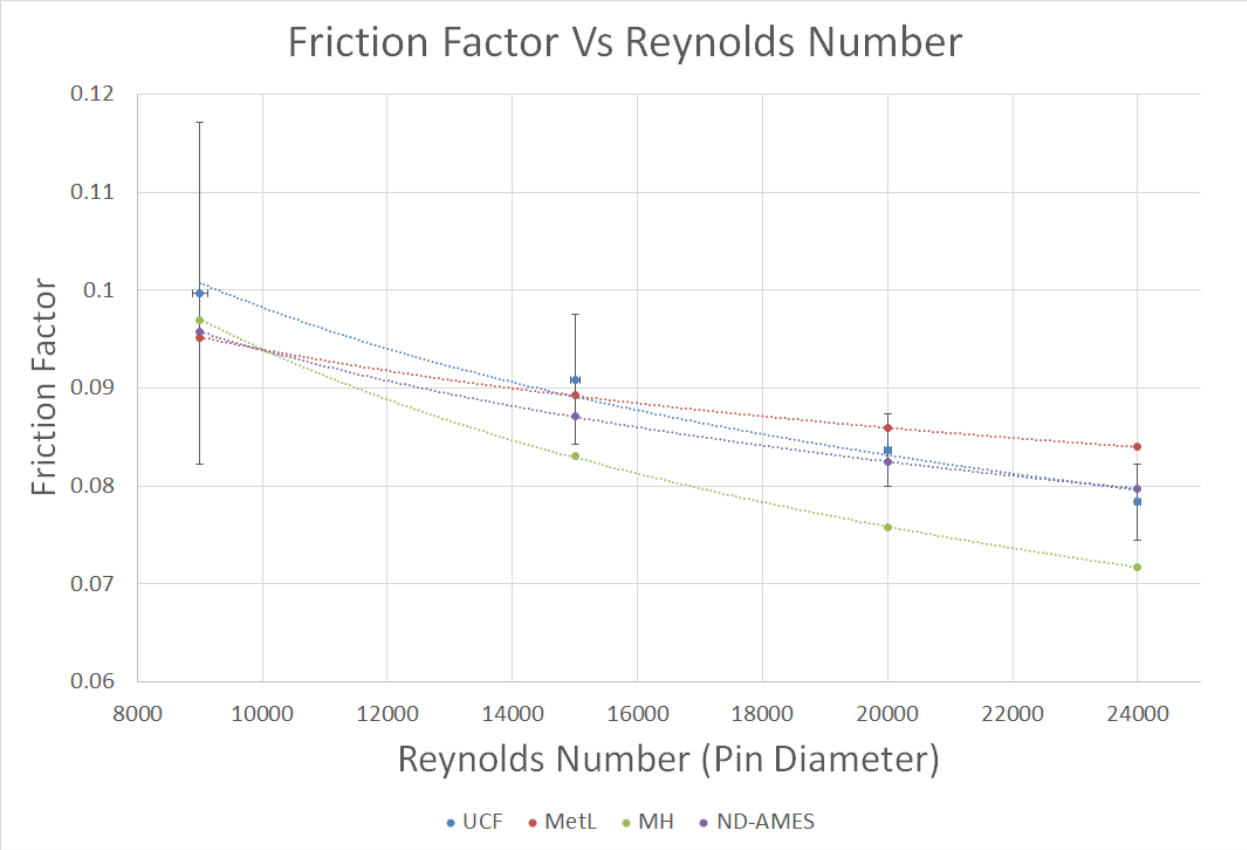

Figure 4.1: Friction Factor Validation

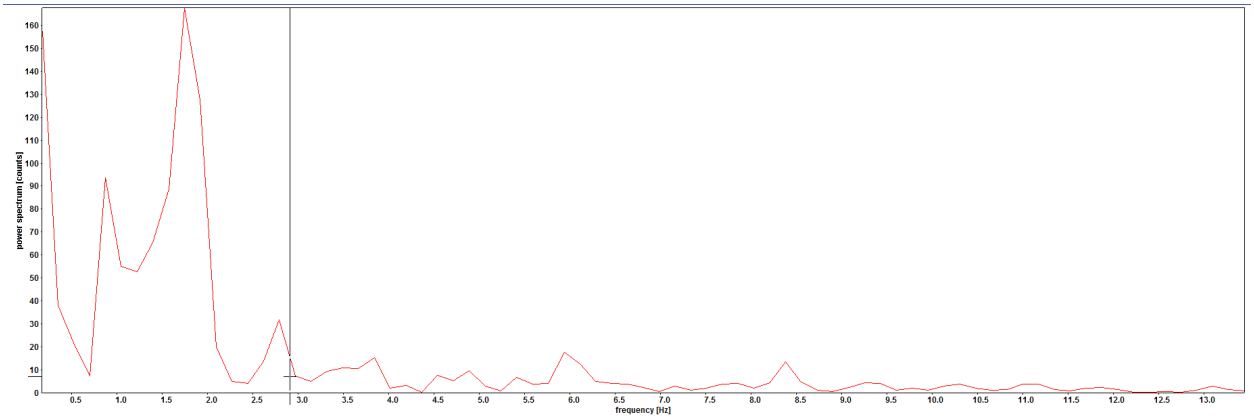

Figure 4.2: Power Spectral Density provided by Proper Orthogonal Decomposition

The Power Spectral Density based on the velocity data show that the Strouhal number is approximately .158, which is similar to that found in literature. The Strouhal number is a non dimensional parameter which quantifies frequency of which the vortex shedding occurs. It is noted that for a single pin, the number is on the order of .2 to .23, however, other reseachers have shown that shedding frequency is between .16-.17 for pin spacing of 2.5.

Table 4.1 show a comparison of friction factor of UCF data compared to other common correlations. Table 3.2 shows the test matrix and their respective channel velocity. There are 3 planes of interest as shown in Figure 3.11, due to symmetry in the flow, it is not necessary to traverse both directions. This is assumed throughout the test and was not measured since the mid plane measurements showed little to no out of plane motion. It is noted that quarter plane is a quarter of the entire test section, however, results in a Z/D of 0.5. Similarly the wall plane results in a Z/D of 0, and mid plane results in Z/D of 1 since the geometry is overall a Z/D of 2.

PIV: Planes of Interest - Test Matrix

Table 4.2: Test Matrix with Mean Velocity

Z/D	Re 10000	Re15000	Re20000	
0	0.228	0.331	0.457	Vmax (m/s)
.5	0.219	0.346	0.458	Vmax (m/s)
1	0.222	0.338	0.46	Vmax (m/s)

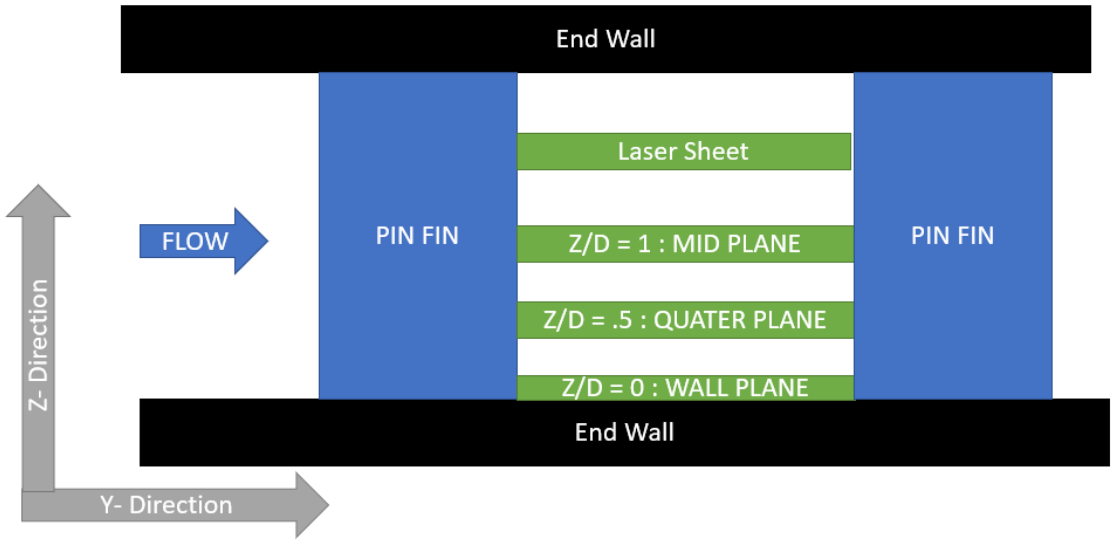

Figure 4.3: Z/D Planes of Interest

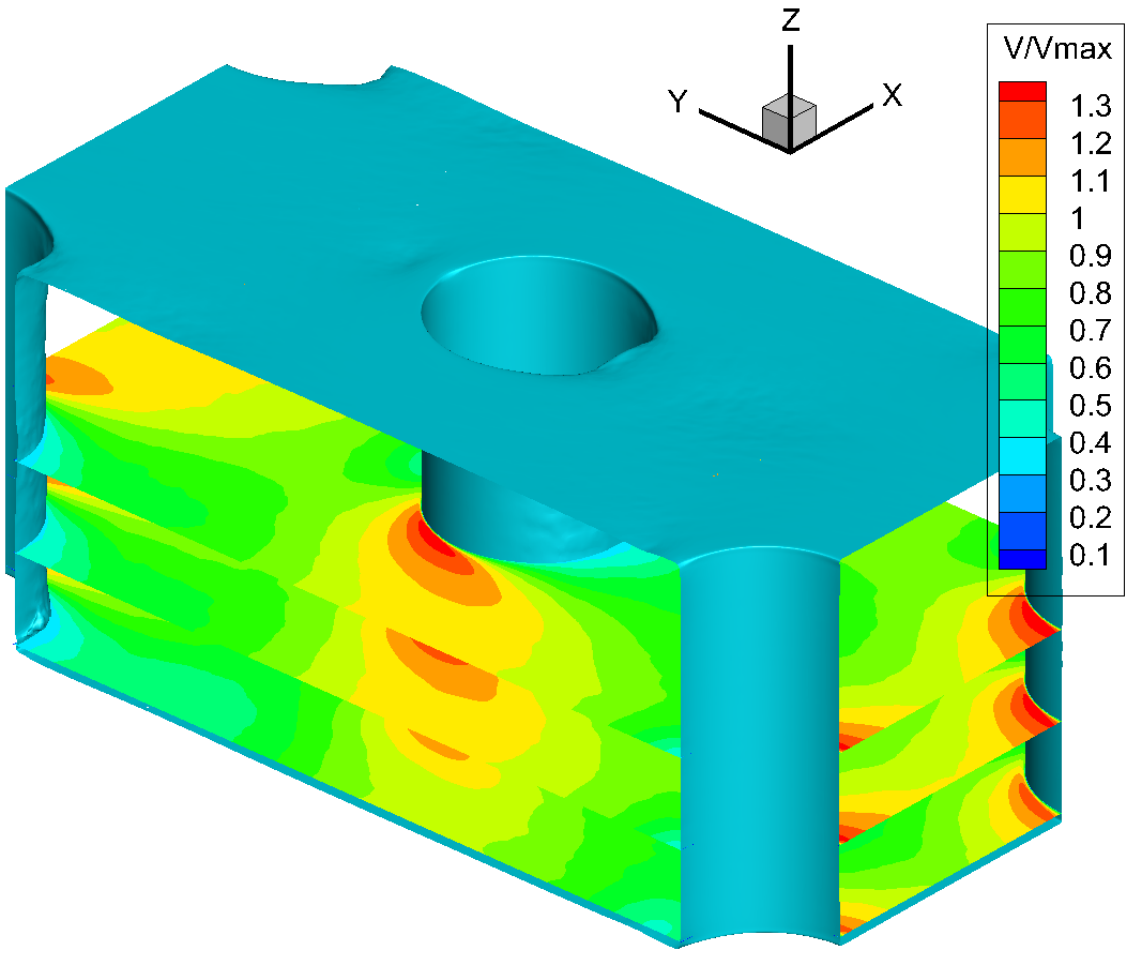

Figure 4.4: Z/D Planes of Interest shown with Respect to CFD

Stereoscopic PIV was used to take velocity field measurements at the mid plane between rows 6 and 7 of the test section. Figures 4.1,4.2 and 4.3 show the flow field velocity with their respective Reynolds number. The velocities are normalized based on Vmax, which is the average velocity based on the minimum area between the pins. It can be seen on all three cases, there is a stagnation point on the front of the pin, suggesting that the flow has come to a complete stop reaching the blunt body and must travel to the side of the pins. Since Stereo PIV was performed, all three components of the velocity vector can be calculated. Figures 4.4, 4.5, and 4.6 show that the out of plane motion or Z direction is nearly 0. Since this is a mid plane measurement, flow is symmetry is expected and can be assumed. It should also be mentioned that the contour of the velocity field suggest that at higher Reynolds number, the flow becomes more uniform around the mean flow, where as the at lower Reynolds number show larger deviations from the normalized velocity. As found in literature, increasing the Reynolds number decreases the distance of re-circulation from the pin. This can be seen from the velocity magnitude from figures 4.5, 4.6, and 4.7 It is noted that the stream lines for all cases are nearly the same, but with different amplitudes. The wake regions come in two pairs, obeying conservation of momentum. Stream lines are added on all plots for easier comparison. Stream lines represent the average flow field velocity direction vector. The magnitude on the stream lines are plotted in Figures 4.5, Figure 4.6, and Figure 4.7.

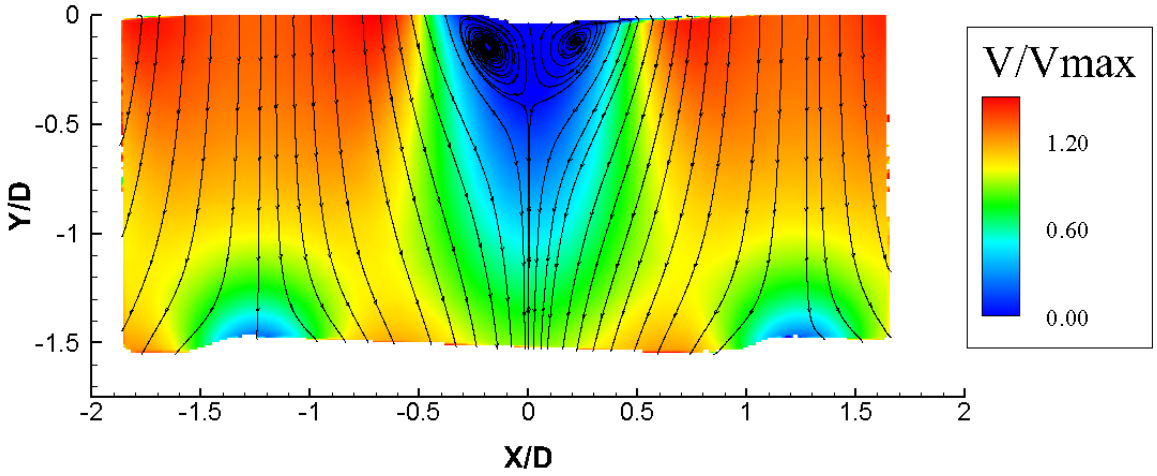

Figure 4.5: Mid Plane Flow Velocity Contour at Reynolds Number 10000

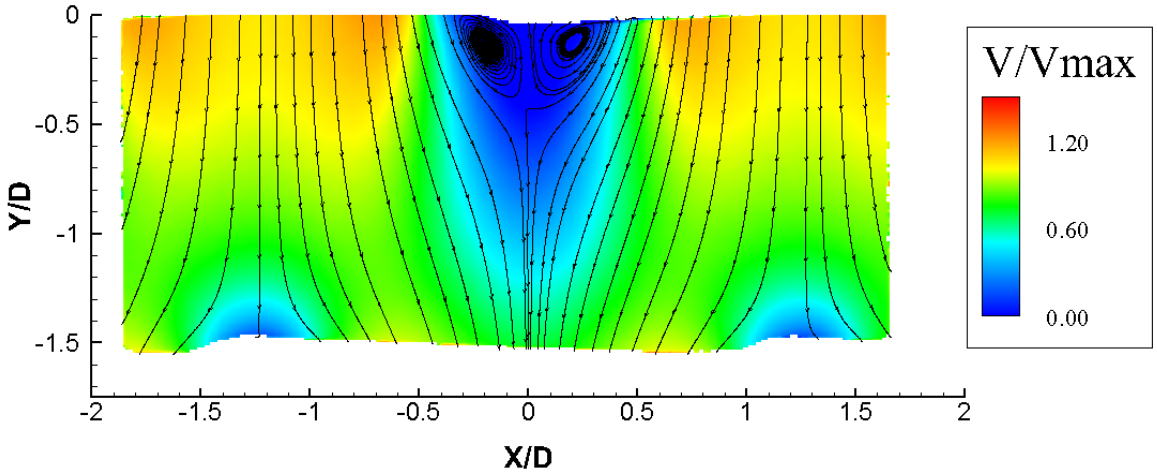

Figure 4.6: Mid Plane Flow Velocity Contour at Reynolds Number 15000

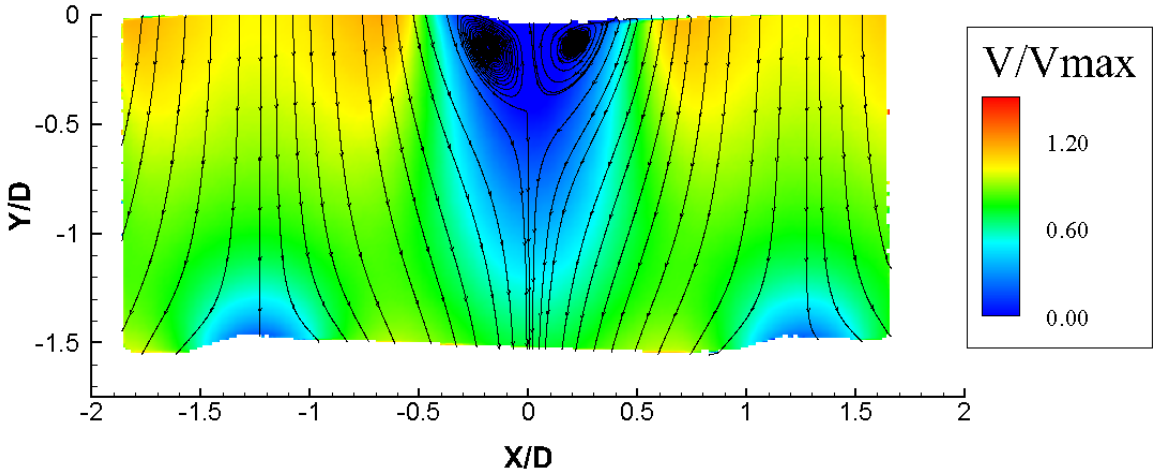

Figure 4.7: Mid Plane Flow Velocity Contour at Reynolds Number 20000

The stereo PIV was performed only on the mid line. Due to the availability of the set up, the Z/D = 0, and Z/D = .5 was not preformed with the stereo method. However, it can be used as a validation of the velocity field with the TR-PIV Set up. As shown in Figure 4.8, Figure 4.9, and Figure 4.10, the out of plane or Z direction is nearly zero, with a faint representing V of 10 % on the bulk velocity which is only the Reynolds number 20,000 Case, shown in figure 4.10. These three plots show the flow is nearly perfectly symmetric in the sense that no out of plane motion is occurring, and is representative of the mid line and maximum velocity of the channel.

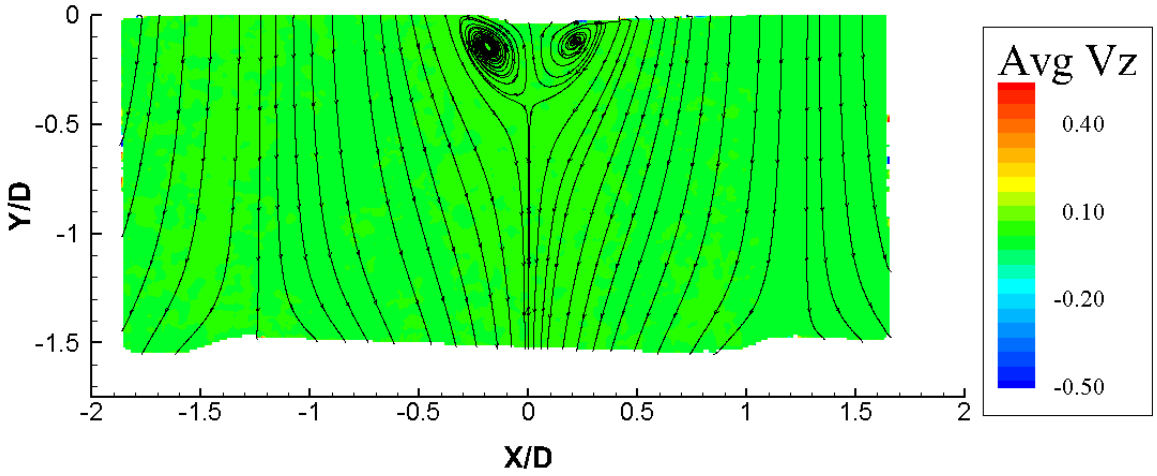

Figure 4.8: Mid Plane Flow Z Velocity Contour at Reynolds 10000

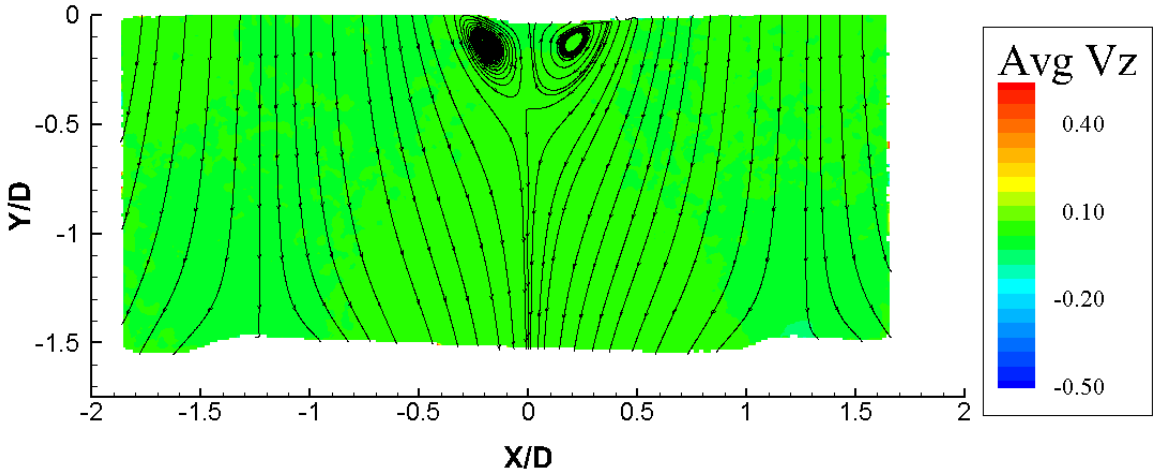

Figure 4.9: Mid Plane Flow Z Velocity Contour at Reynolds 15000

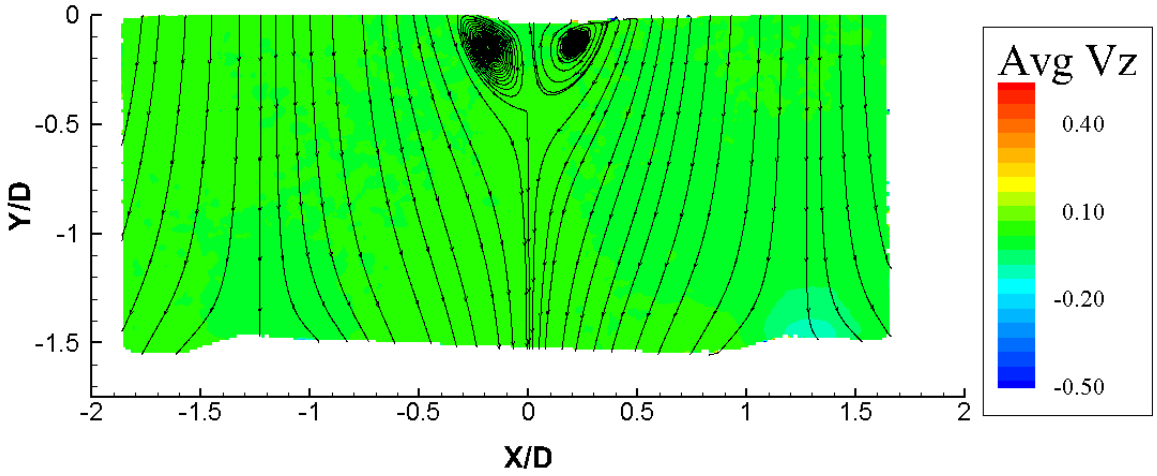

Figure 4.10: Mid Plane Flow Z Velocity Contour at Reynolds 20000

The use of total kinetic energy can show where the bulk on the flow will contain the majority of the turbulence, higher levels of kinetic energy leads to destabilization of streamlines which in turn causes eddies to dissipate that energy. Figure 4.11, 4.12, and 4.13 show that the accelerating flow around the pin has the majority of the energy as well as not the wake region, but not immediately in the re-circulation region of behind the pin. The plots are normalized by of the Total Turbulent Kinetic energy divided by the square of Vmax. It can be shown that the relative TKE in much higher in magnitude in the lower Reynolds number cases, with a effuses that maximum TKE in outside of the re-circulation zone, into the wake region and areas of the VK vortex. Other than the vortex area and re-circulation zone, the bulk velocity in the middle of the pin show very low turbulence level. All three contours show that the highest levels of TKE appear slightly after the pin, and decreases in magnitude in the streamline. Figure 4.14, Figure 4.15, and Figure 4.16 show the vorticity in the Z-plane, which correlates almost exactly in the with the locations high high TKE. However, the TKE extends well into the vortex shedding region as well.

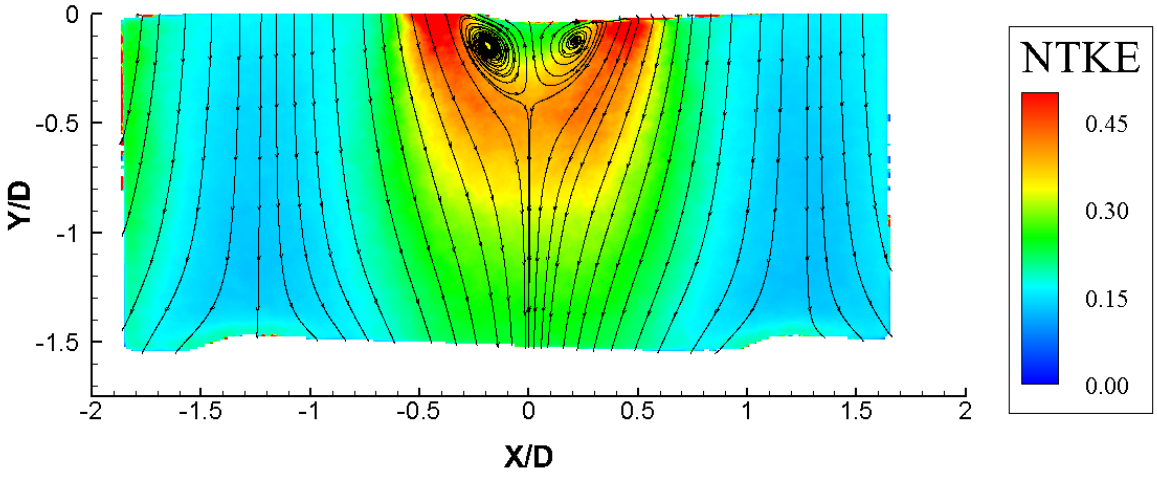

Figure 4.11: Mid Plane Flow Turbulent Kinetic Energy Contour at Reynolds Number 10000

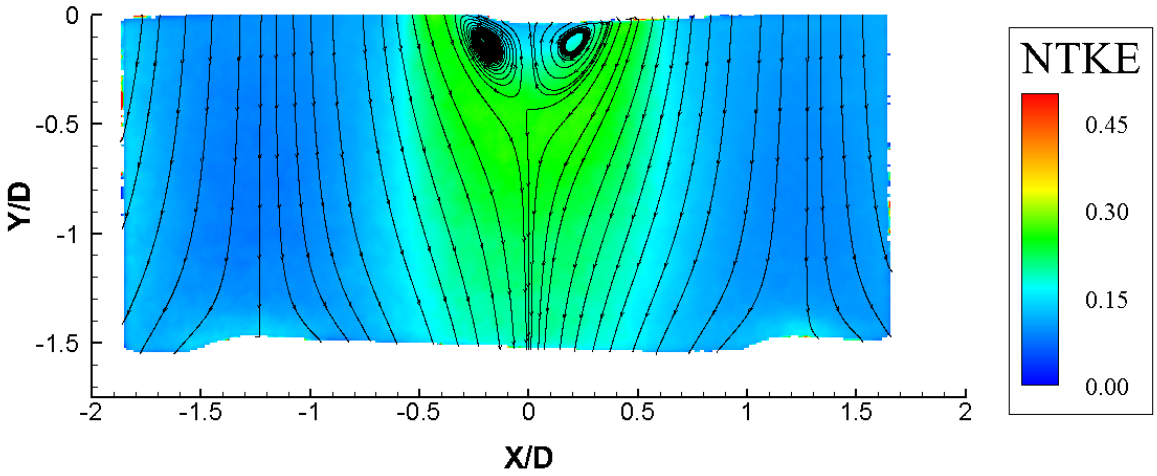

Figure 4.12: Mid Plane Flow Turbulent Kinetic Energy Contour at Reynolds Number 15000

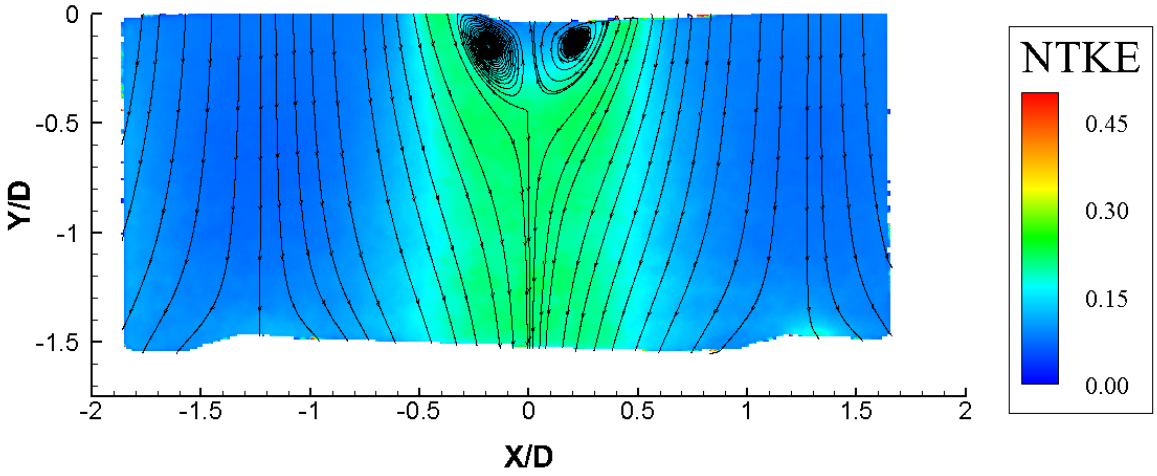

Figure 4.13: Mid Plane Flow Turbulent Kinetic Energy Contour at Reynolds Number 20000

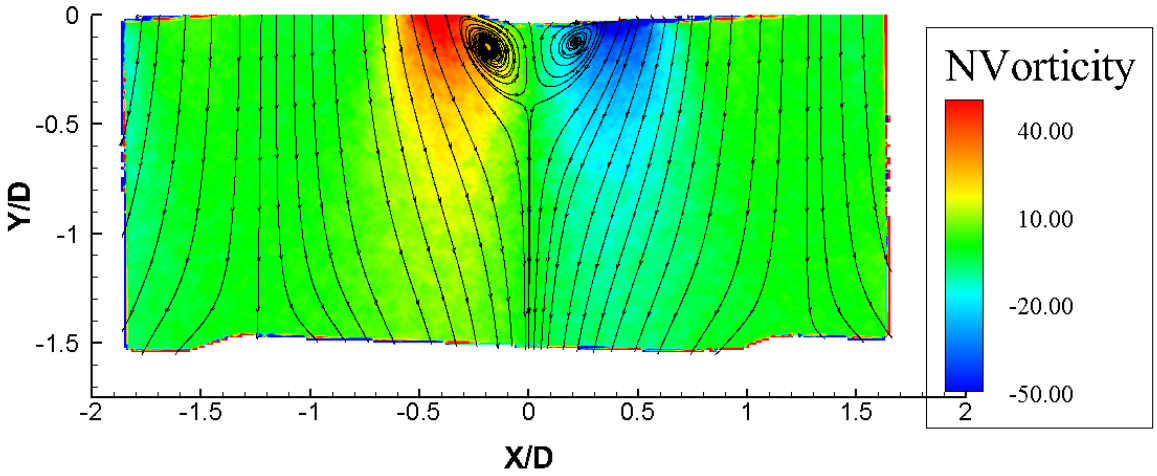

Figure 4.14: Mid Plane Time averaged Vorticity Contour at Reynolds Number 10000

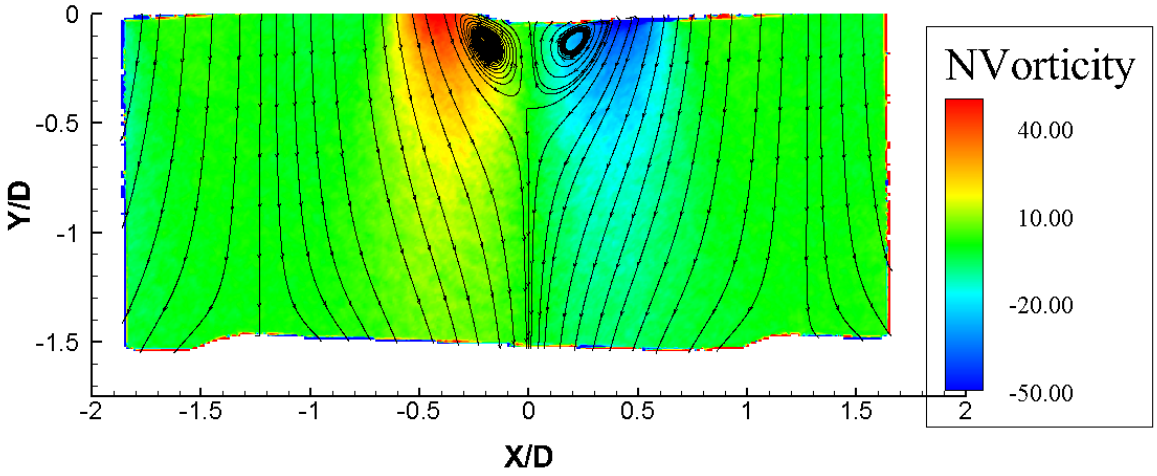

Figure 4.15: Mid Plane Flow Turbulent Kinetic Energy Contour at Reynolds Number 15000

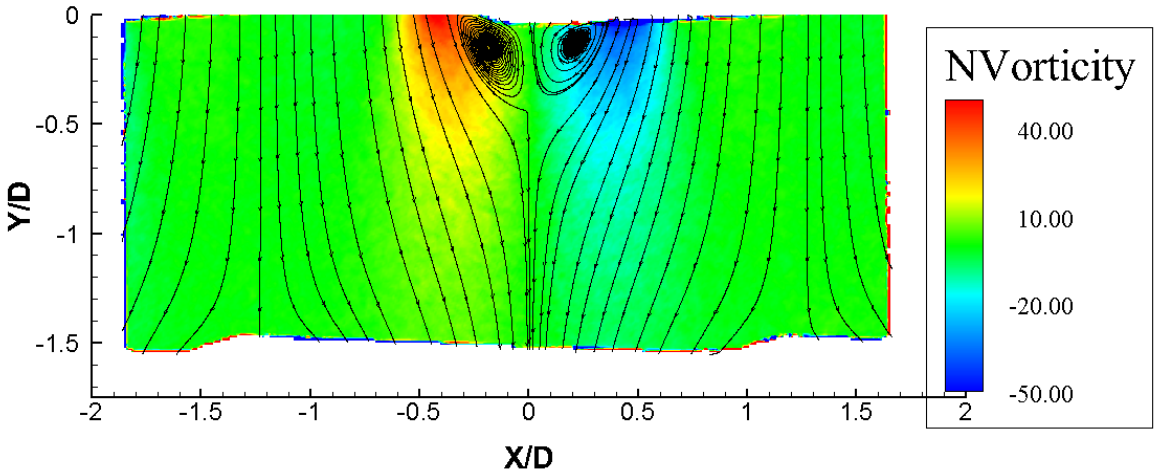

Figure 4.16: Mid Plane Flow Turbulent Kinetic Energy Contour at Reynolds Number 20000

Similarly shear stress in the main provider of flow motion. The definition of fluids is that a body of particles is able to continuously deform when a force is applied. Areas of high shear stress as shown in figures 4.17, 4.18, and 4.19 show the XX direction of shear stress. Similarly Figures 4.20, 4.21, and 4.22 show the YY direction. It is clear that the shear in the YY direction is orders of magnitude higher than the XX direction. This means that the majority of the force is being applied to move the fluid in the stream-wise direction compared to the span-wise direction. Figures 4.23, 4.24, and 4.25 show the ZZ direction, however, besides the Reynolds number of 20,000, the shear stress is nearly 0.

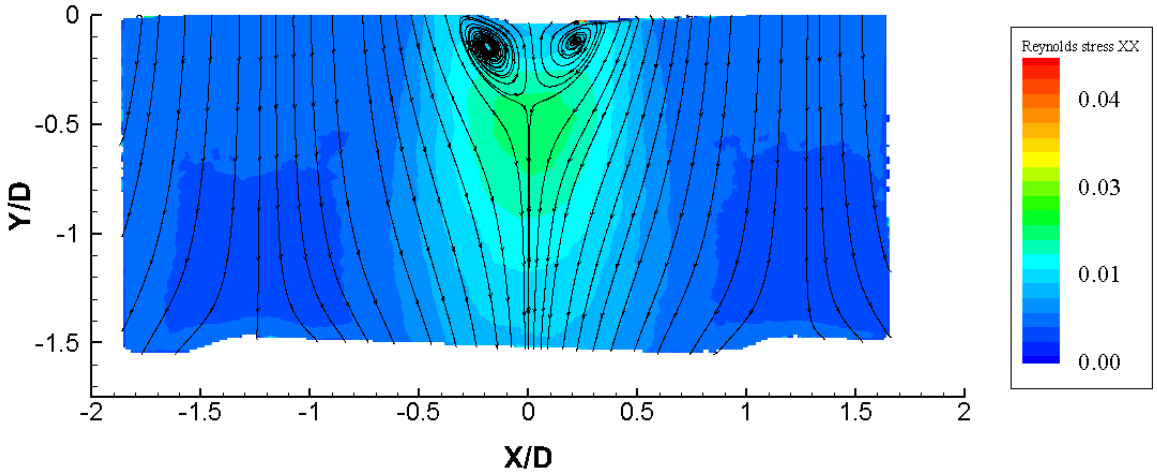

Figure 4.17: Mid Plane Flow XX Reynolds Shear Stress at Reynolds 10000

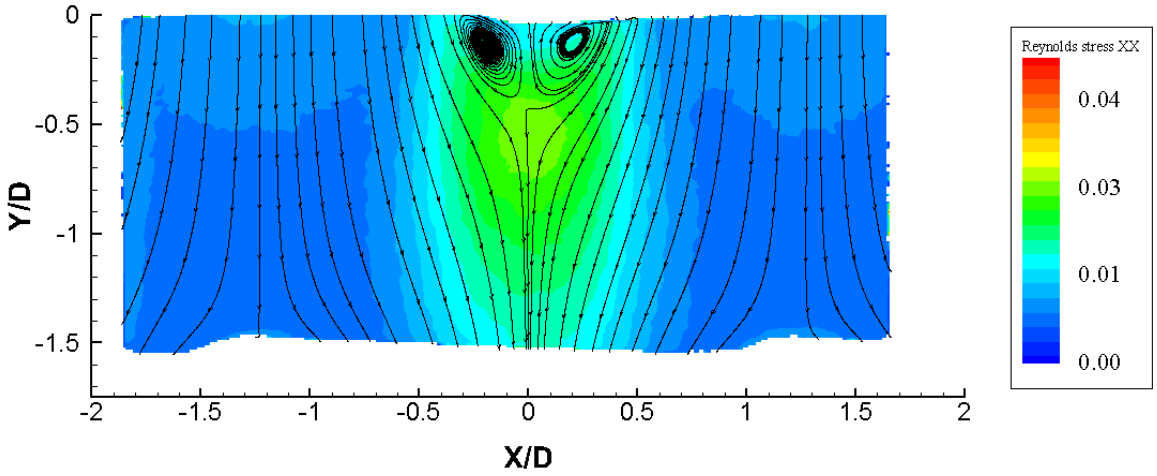

Figure 4.18: Mid Plane Flow XX Reynolds Shear Stress at Reynolds 15000

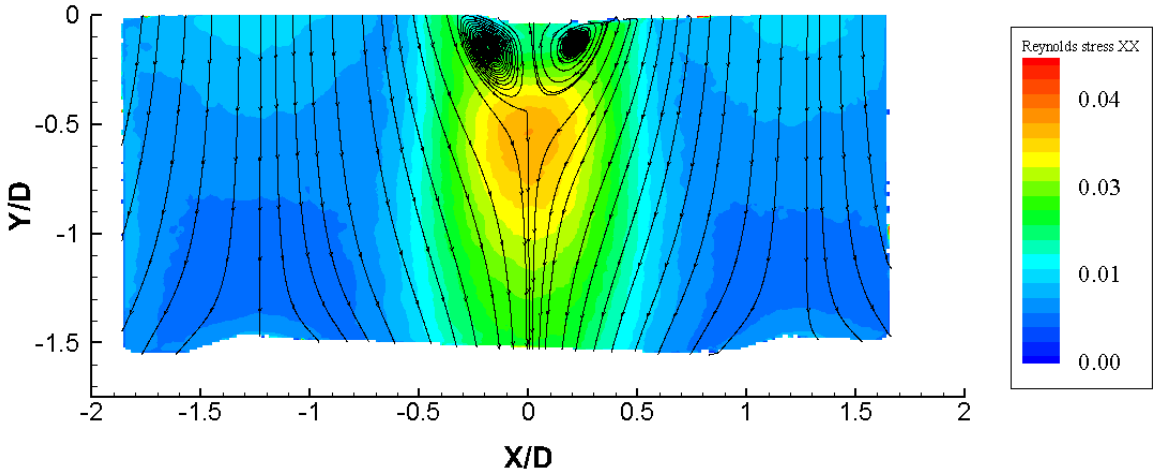

Figure 4.19: Mid Plane Flow XX Reynolds Shear Stress at Reynolds 20000

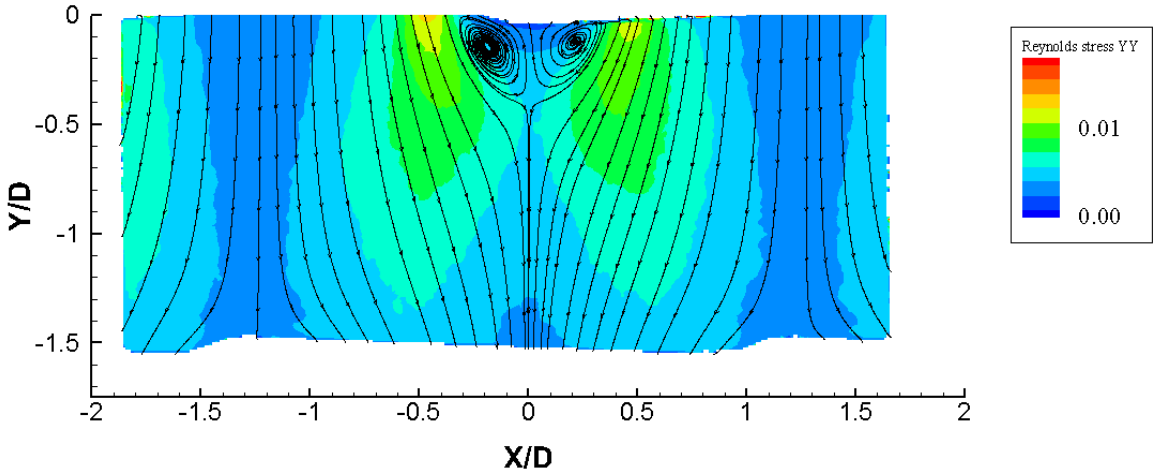

Figure 4.20: Mid Plane Flow YY Reynolds Shear Stress at Reynolds 10000

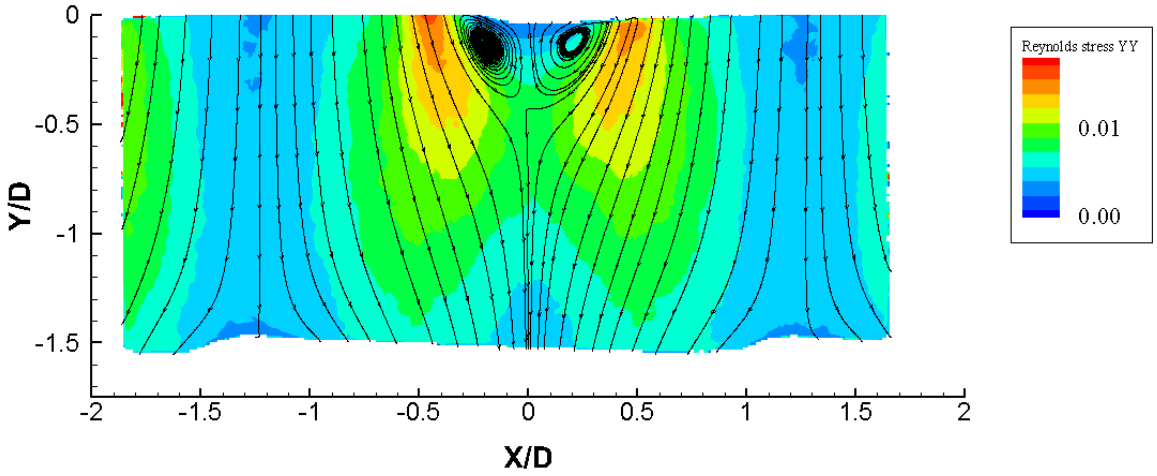

Figure 4.21: Mid Plane Flow YY Reynolds Shear Stress at Reynolds 15000

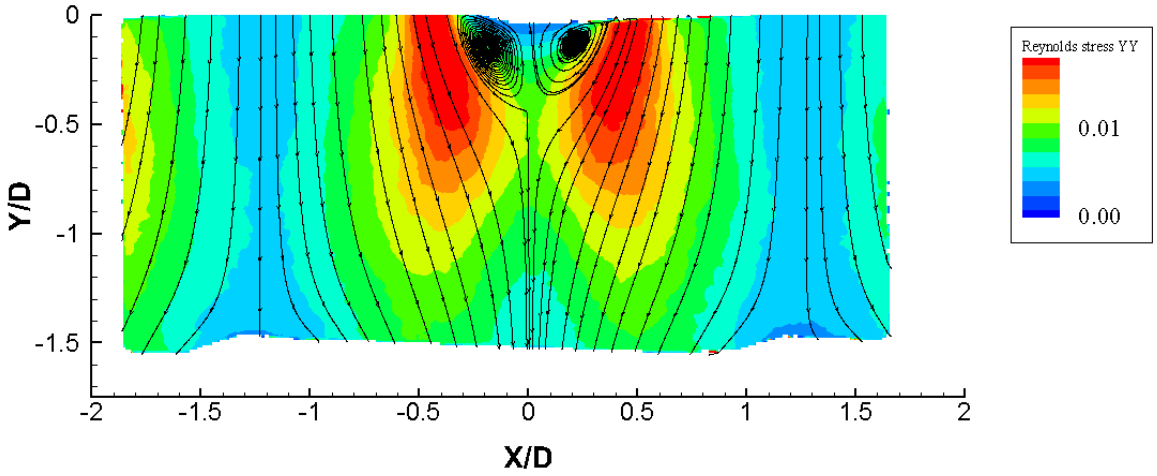

Figure 4.22: Mid Plane Flow YY Reynolds Shear Stress at Reynolds 10000

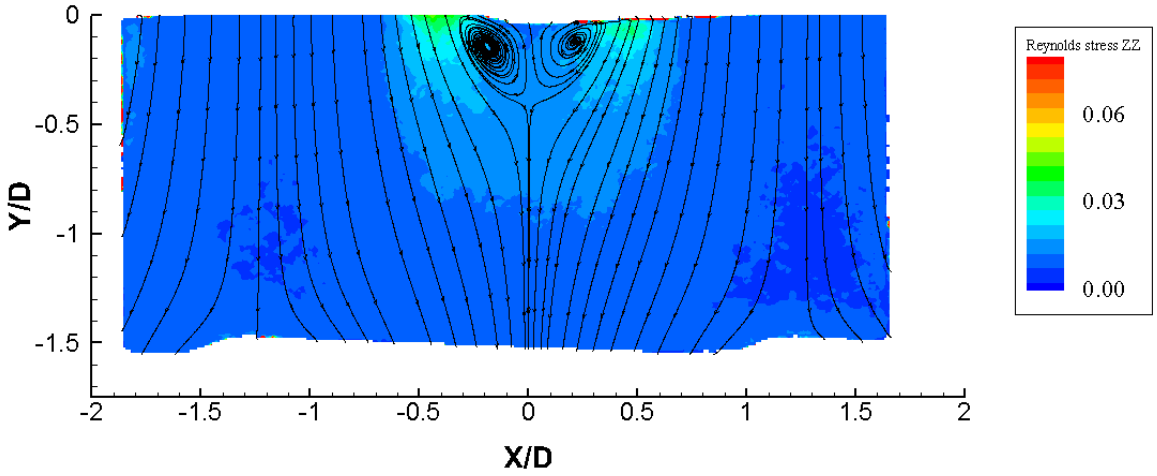

Figure 4.23: Mid Plane Flow ZZ Reynolds Shear Stress at Reynolds 10000

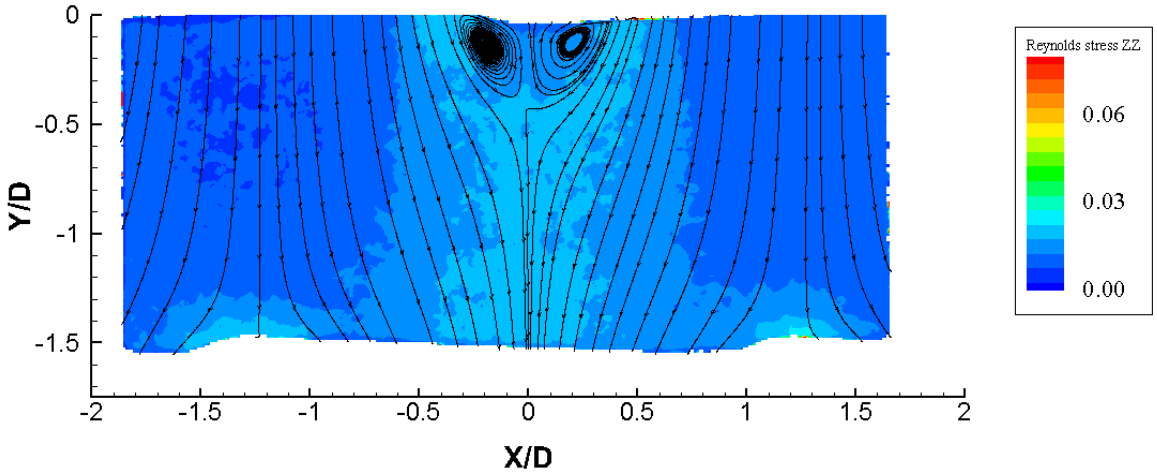

Figure 4.24: Mid Plane Flow ZZ Reynolds Shear Stress at Reynolds 15000

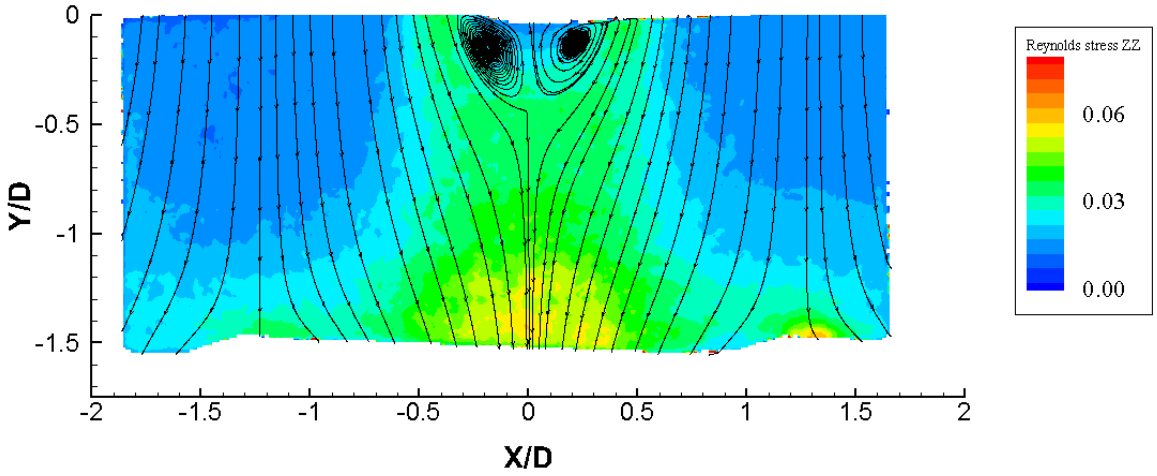

Figure 4.25: Mid Plane Flow ZZ Reynolds Shear Stress at Reynolds 20000

CFD

A steady and unsteady simulation has been completed and is only part of this study. A mesh dependence study was performed with the a 3 million, 5 million, 7 million, and 9 million cells mesh. It was found that 5.1 million cells were enough to capture the average flow field parameters. The LES study was performed with a cell count of 14.8 million cells. A steady Reynolds Average Navier Stokes (RANS) with a k-w model with gravity was performed until the mesh converged. Figures 4.27, 4.28, and 4.29 show comparison of the steady CFD results with the PIV data. It is found that the wake region is predicted, however, the vortex shedding length is over predicted by CFD. In terms of the velocity contours, the magnitudes show very similar values. In Figure 4.30, and unsteady CFD comparison is shown as well. However, in the unsteady case, the vortex shedding is more prominent, but the trends velocity values and regions are nearly the same. A few line traces are provided by an LES CFD study in the following plots as well.

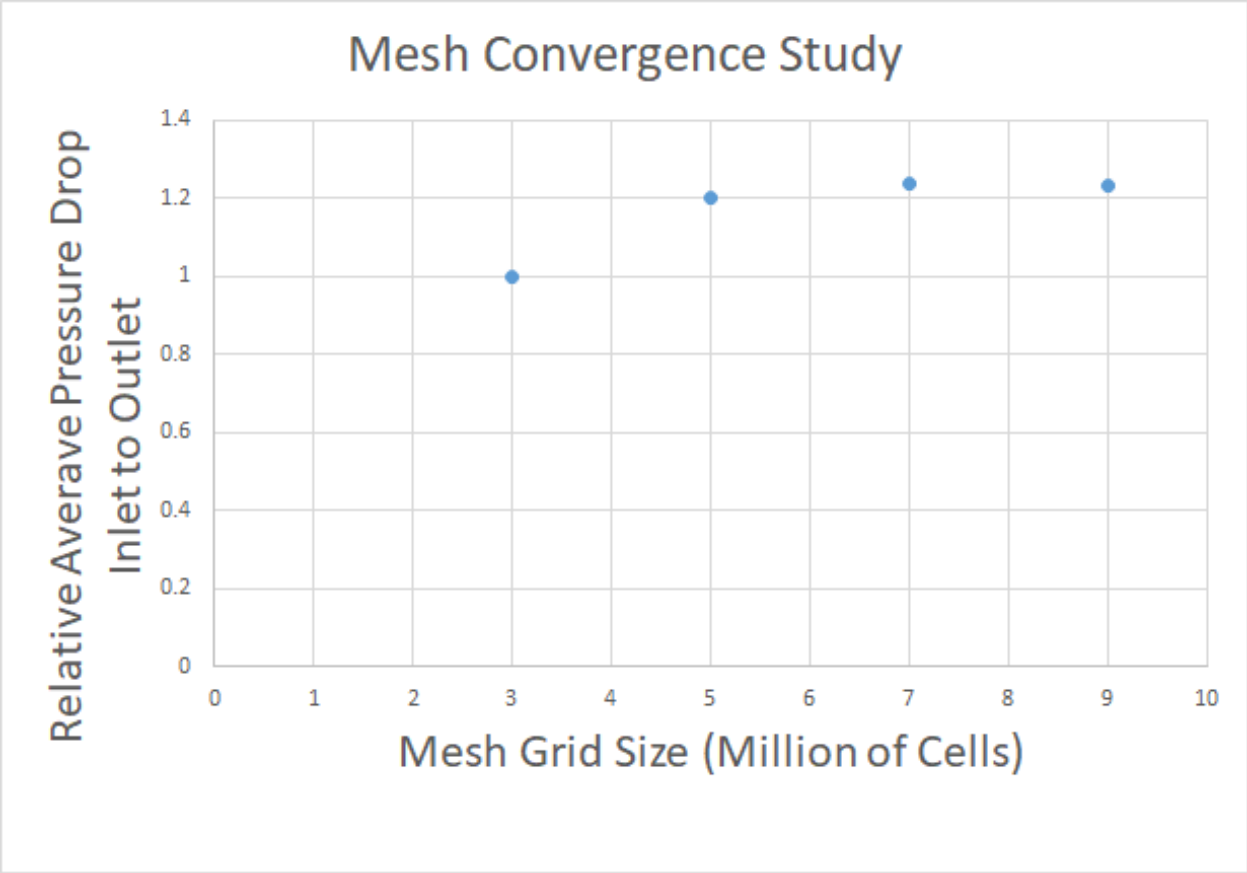

Figure 4.26: CFD Grid convergence study

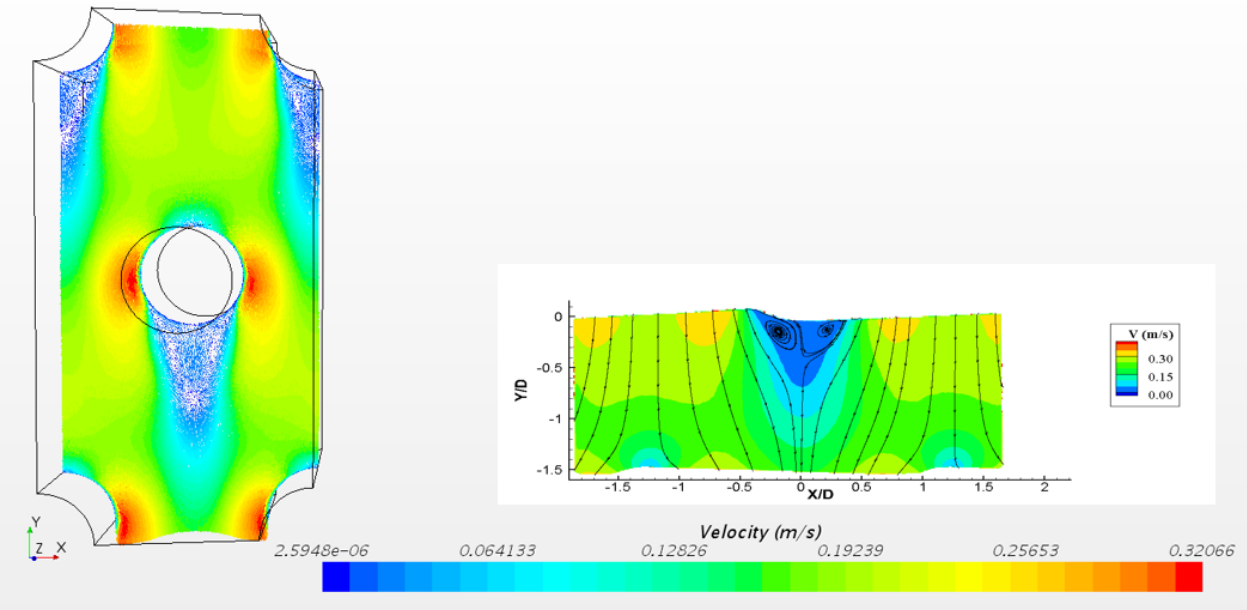

Figure 4.27: Reynolds Number 10000 Flow Simulation

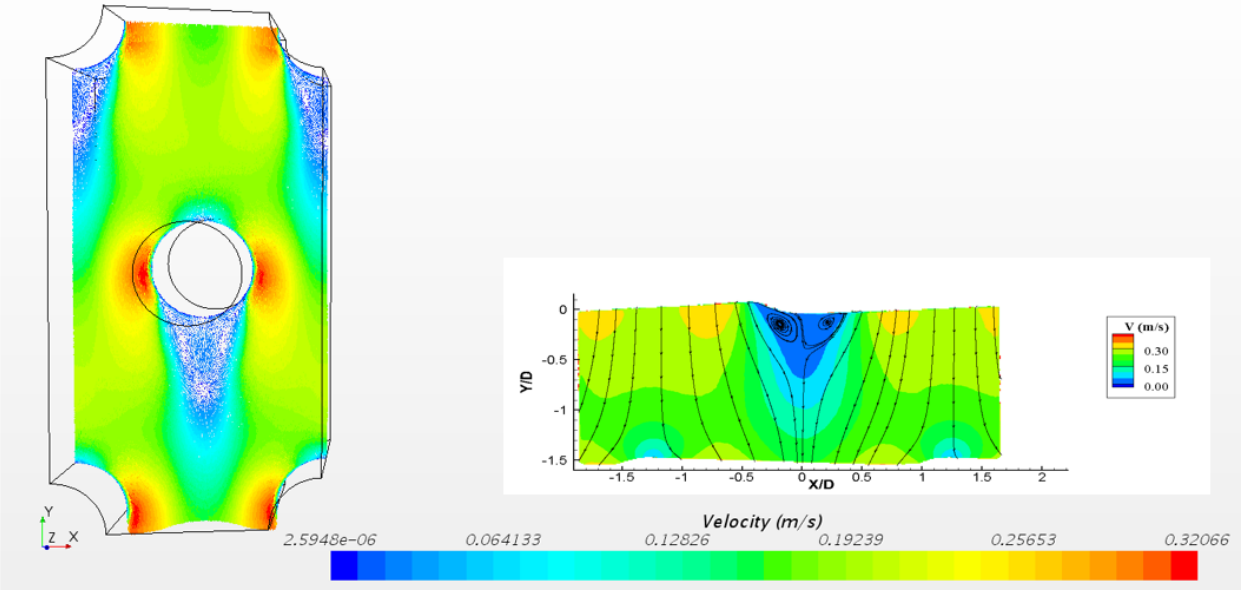

Figure 4.28: Reynolds Number 15000 Flow Simulation

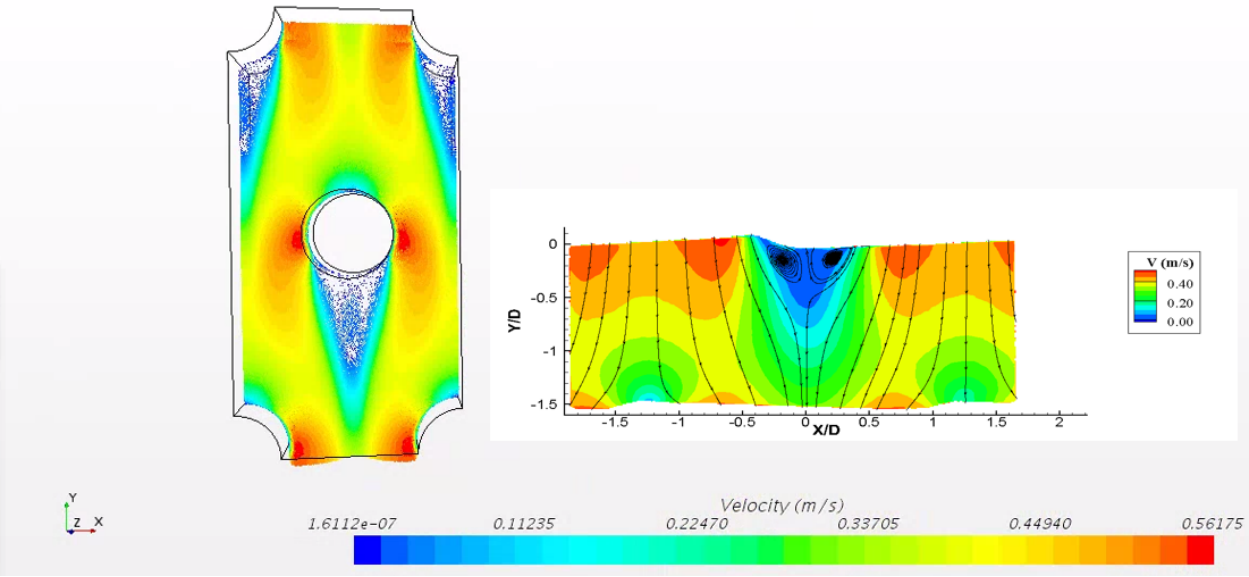

Figure 4.29: Reynolds Number 20000 Flow Simulation

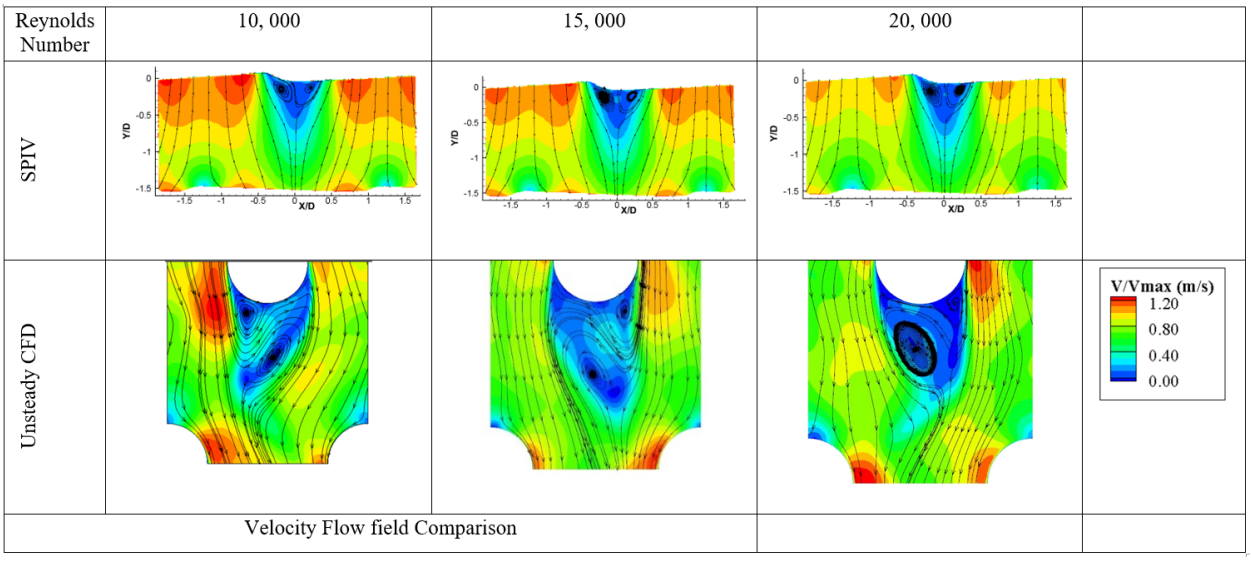

Figure 4.30: Unstready CFD Comparison

Comparison with CFD show that the velocity magnitude and direction are identical span wise to the pin. However, the re-circulation zone is heavily over predicted by the model. The re-circulation zone in the PIV data is nearly half a pin diameter, where the CFD show the circulation zone past one full diameter. The stream wise velocity other than that show agree well with each other.

Large Eddy Simulation (LES)

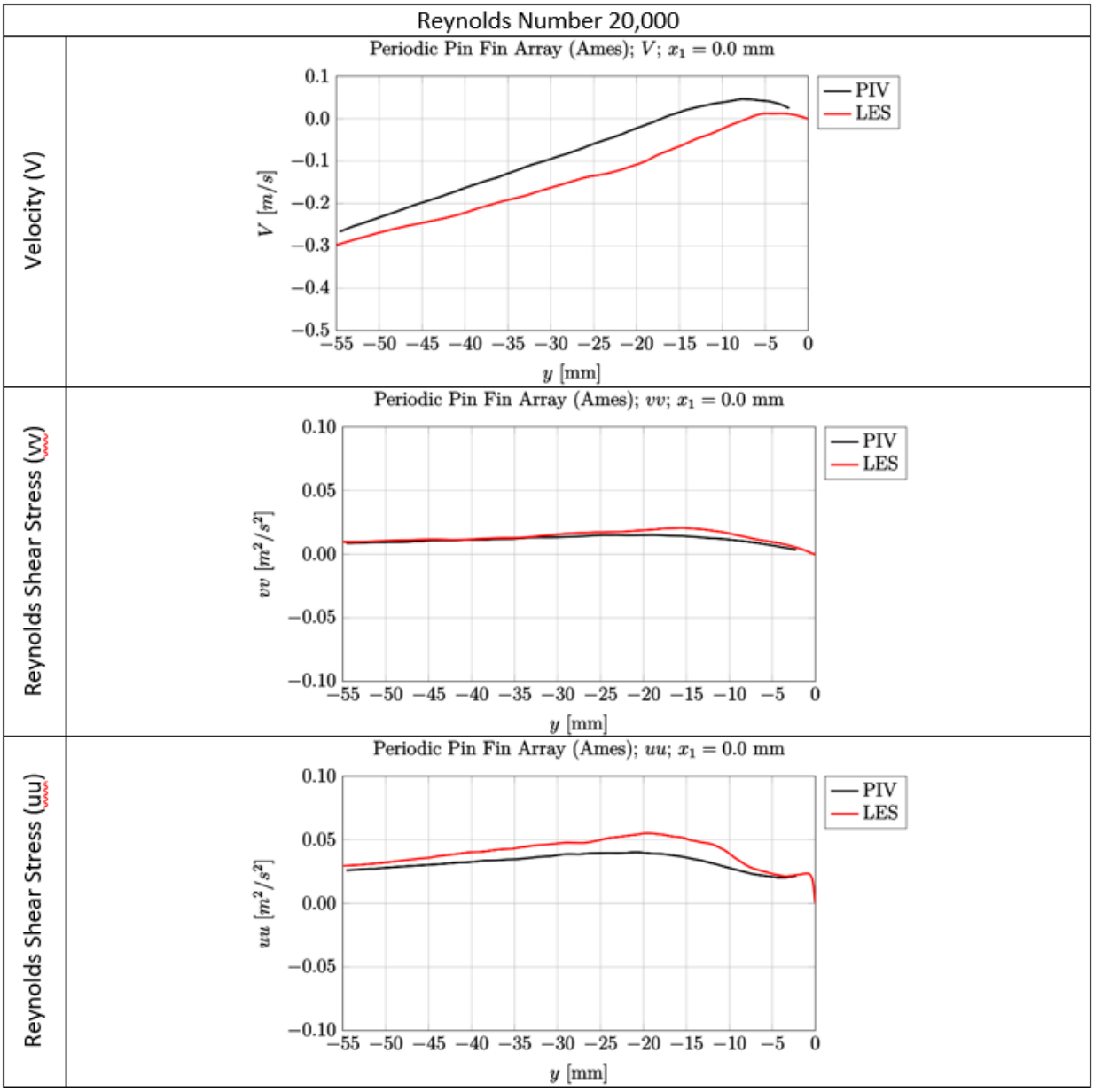

Figure 4.31: PIV Validation with LES

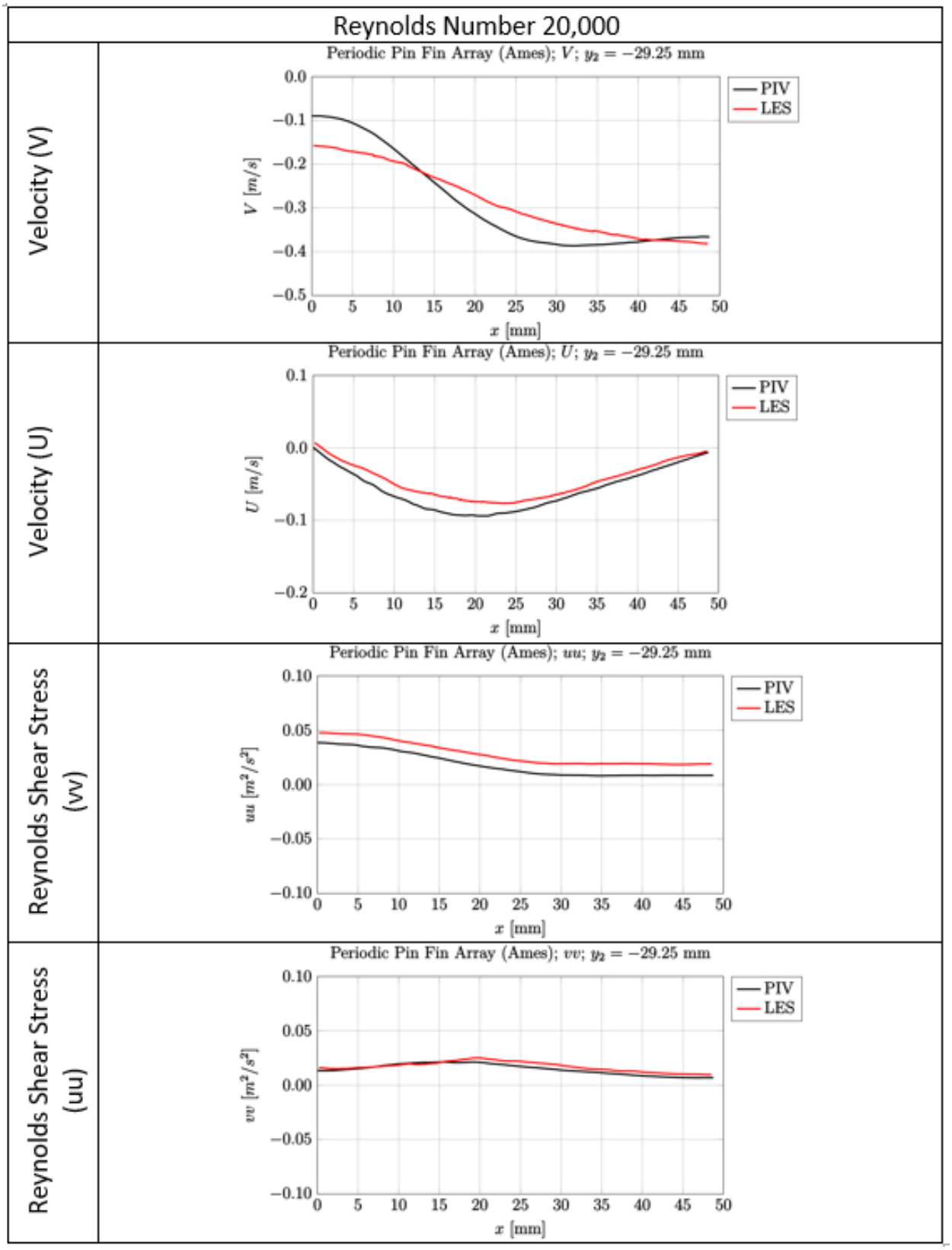

Figure 4.32: PIV Validation with LES

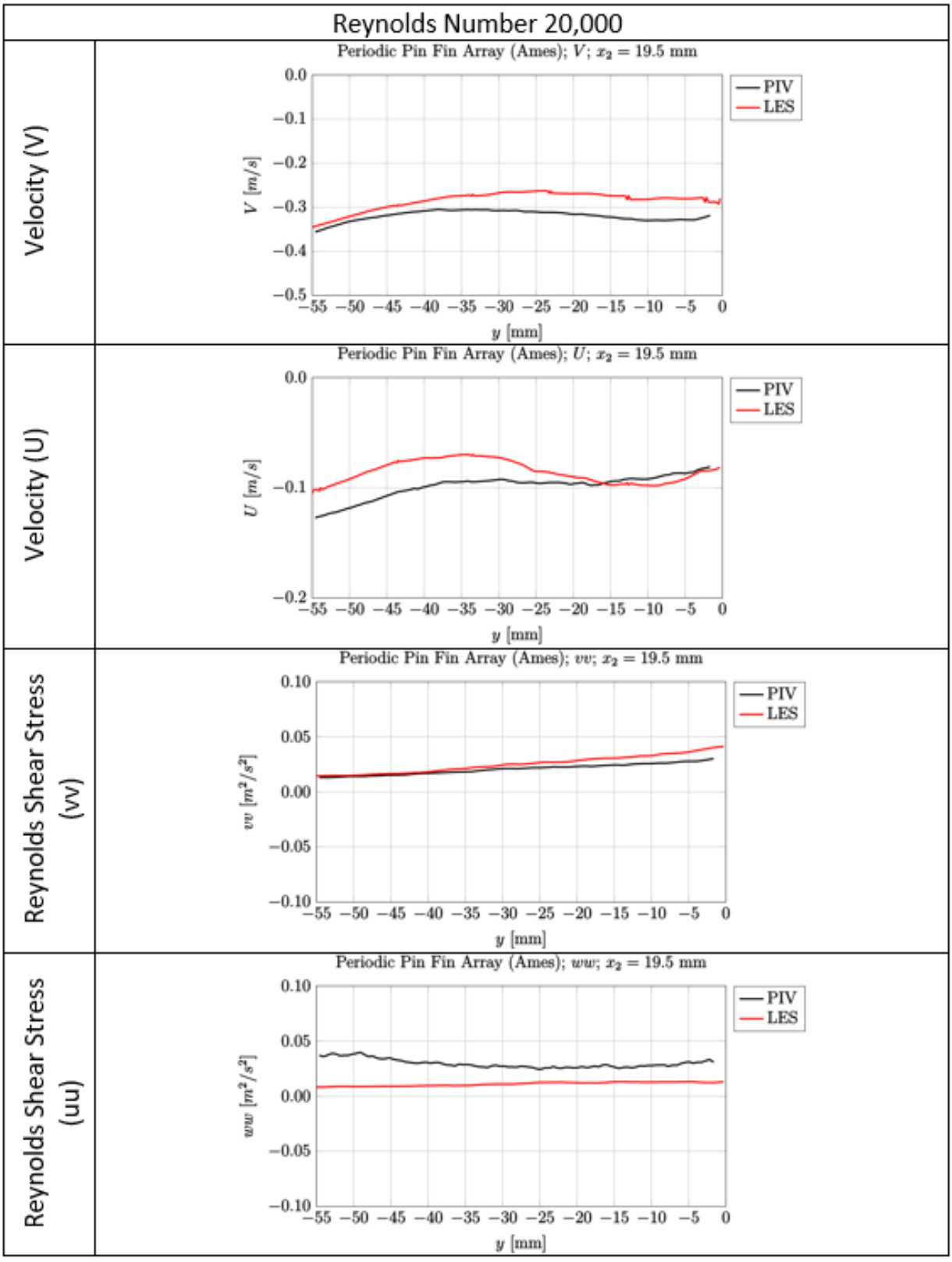

Figure 4.33: PIV Validation with LES

The large eddy simulation showed promising results, however, some areas of the flow are still not predicted. Taking a line trace a at X/D = 0, the velocity is slightly under predicted, however the trends of the velocity profile match. Only the V direction component of velocity profile is plotted, as the X direction velocity is zero at the center line and is uninteresting. It can be seen the that Reynolds stress components strongly agree between the experiment and the simulation. However, at X/D = 1.25 the U component of velocity seen to be over predicted, suggesting that the simulation is predicting a vortex structure is further away from the span wise direction than expected. This result shows that the spatial location of a vortex might be misaligned slightly, The underproduction can be seen the the Reynolds stress as well. The uu component in the Simulation was over predicted, suggesting that flow is accelerating span wise, where it is not seen in the experiment. Moving forward to the Y/D = 1.25 direction and taking the line trace as well, it can be seen that LES shows a linear decay in velocity where PIV suggest that the bulk flow from the previous pin spacing does not penetrate the von Karmon Vortex or reconciliation area.

Velocity Modes

A modal analysis based on the velocity is presented as well. Once the velocity vectors are processed, the number of occurrences for each velocity in the Y direction can be plotted in a histogram. This process is known as a modal probability density function. Based on the occurrences, it shows which velocity vectors are dominate in the flow field. If there are multiple vortex structures, the modal distribution will have multiple peaks, if the flow is uniform with no vortex, than only the bulk free stream Gaussian peak occurs. Flow pattern that have two distinct distribution are called U shaped distribution, and sometimes called bi-modal distribution, that is the flow contains 2 major vortex structures alongside the free stream, and can increase to multi modal shapes if more than two are found. In Figures 4.34, Figure 4.35, and Figure 4.36, the main modal peaks are plotted in increments of 10 % the Strouhal number of the flow. Given the various

shape, an estimation of the flow field can be expected. These plots aid finding the expected number of vortex structure, as well as the expected magnitude around that vortex structure. However, a Q-Criteria plot is more helpful in finding the spatial location on the vortex. The modal plots are provide in a sense to convey a first pass of finding the number of mode shapes to expect within the wake region. It can be seen that at lower Reynolds number the band is much tighter. That is the min and max values are lower in range. It is also found that at higher Reynolds number, the effective number of peaks increase, increasing the number of vortex structures found. It is found that at lower flow rates or Reynolds number, contain the least amount peak, and sometimes contain a Gaussian distributions. A pure Gaussian with no negative values represent a flow that has no vortex structures, and contains a bulk flow with a peak velocity of the highest recorded velocity on the histogram. The peak value of this Gaussian histogram also represents the mean velocity, which in turn in the bulk velocity of the flow, which is also near the Vmax value used to calculated the Reynolds number. All Z/D = 0 cases of the histogram should be compared to Z/D = .5. All other histograms of Z/D = .5 and Z/D = 1 show similar results. A large range of values in velocity as well as many peaks. These plots should convince the reader that planes outside of Z/D =0 are heavily influences by other vortex structures. For instance, Z/D = .5 could be heavily influence by HSV and mid line by wake and vortex shedding. Plots of time average results for the other planes of interest are shown in Figure 4.38. It is noted that the horseshoe vortex is found in all cases of Z/D = 0. A strong indicator of this is a very low normalized velocity at the Z/D planes and that feature it not found in the other case near the leading edge of the pin. It is also noted that at lower Reynolds number the flow relative to the Vmax definition varies much more compared to the other Reynolds number.

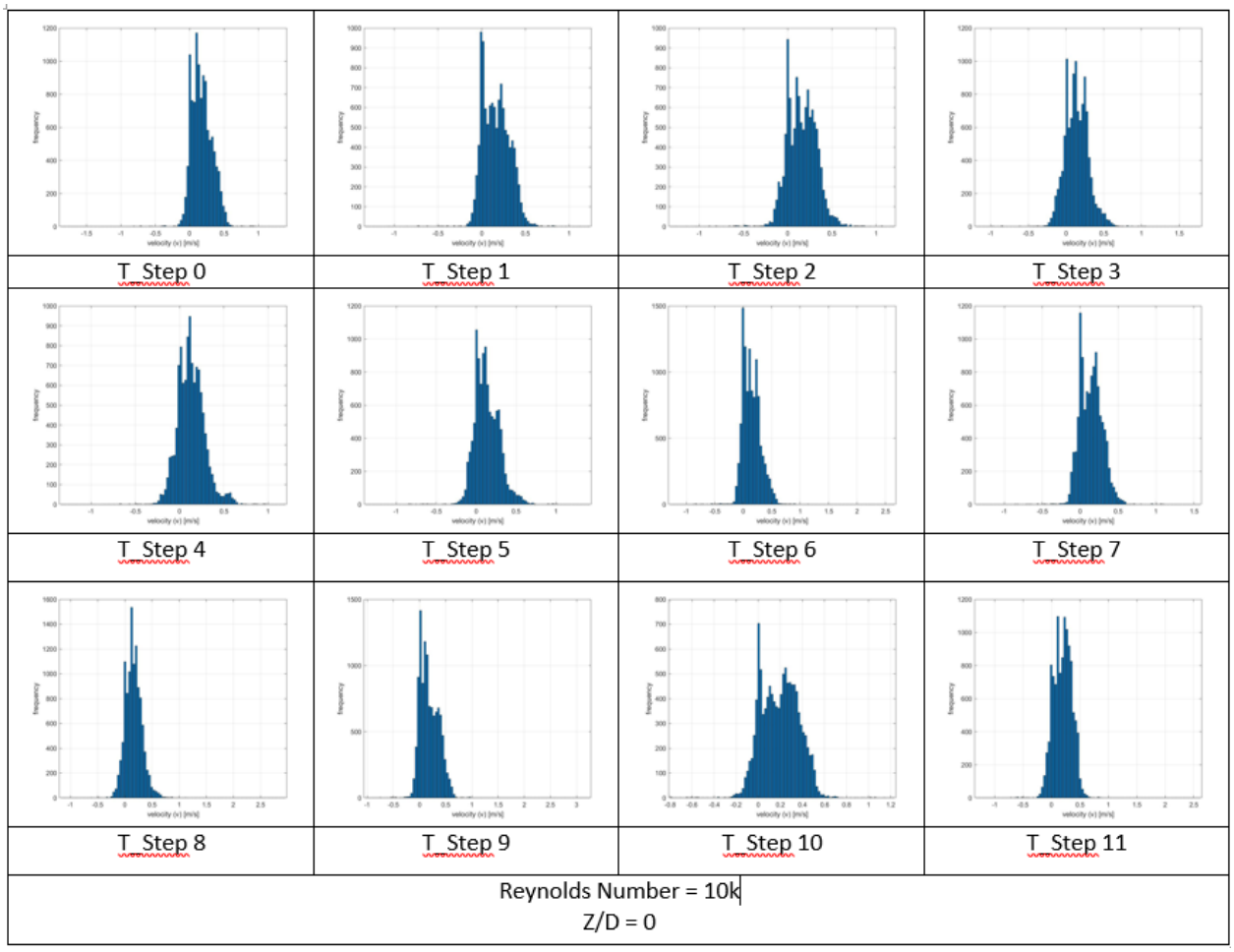

Figure 4.34: Velocity Histogram for Reynolds number 10000 at Z/D = 0

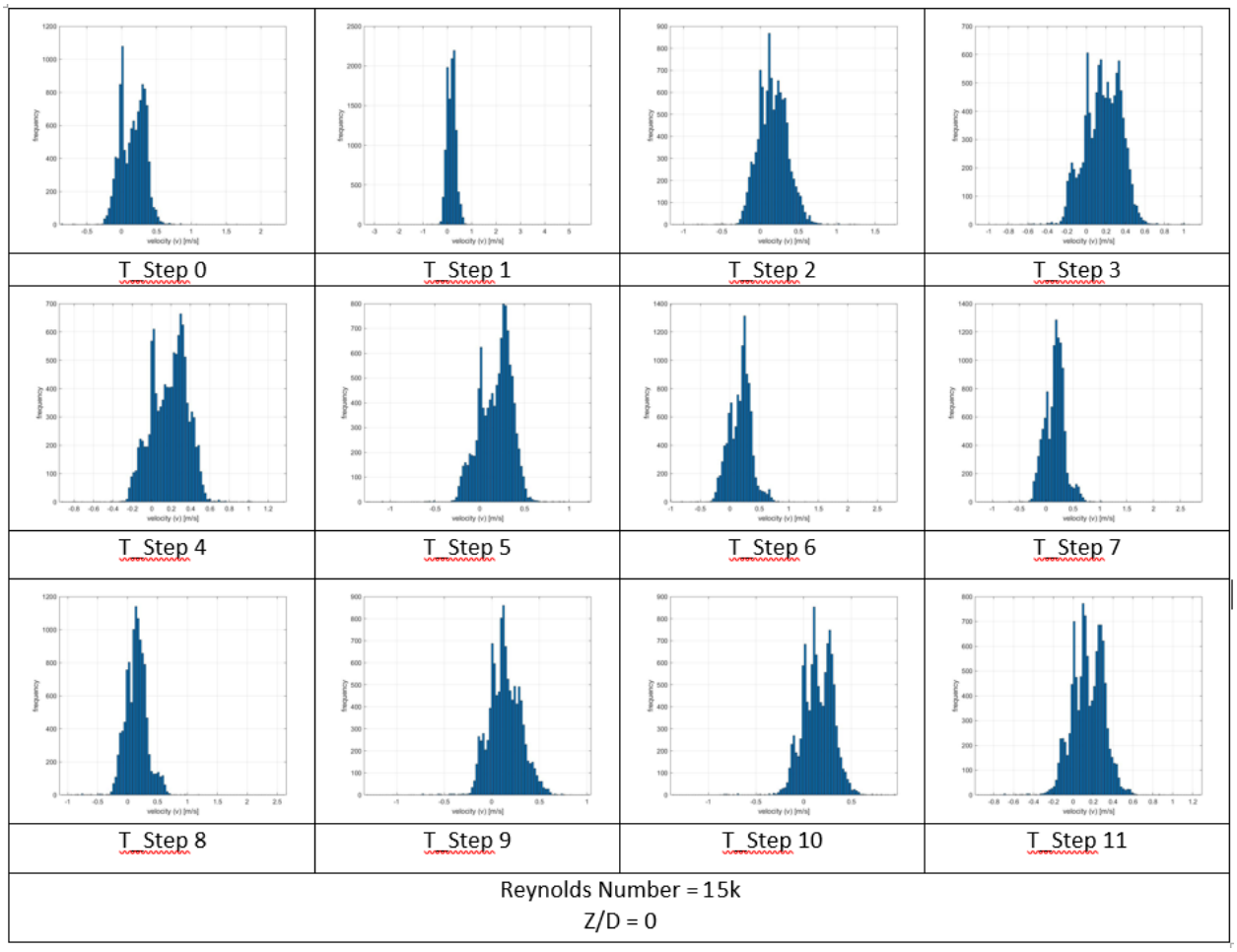

Figure 4.35: Velocity Histogram for Reynolds number 15000 at Z/D = 0

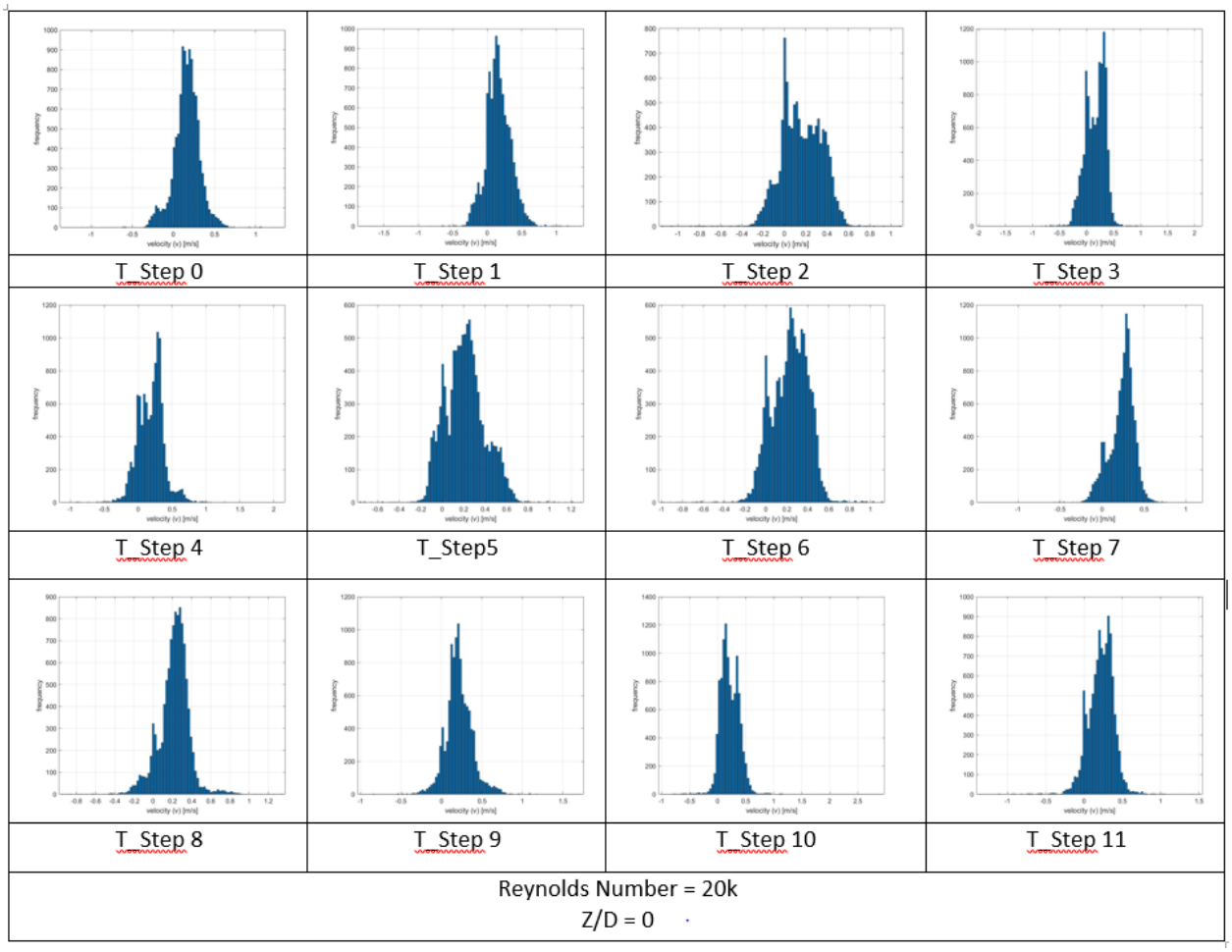

Figure 4.36: Velocity Histogram for Reynolds number 20000 at Z/D = 0

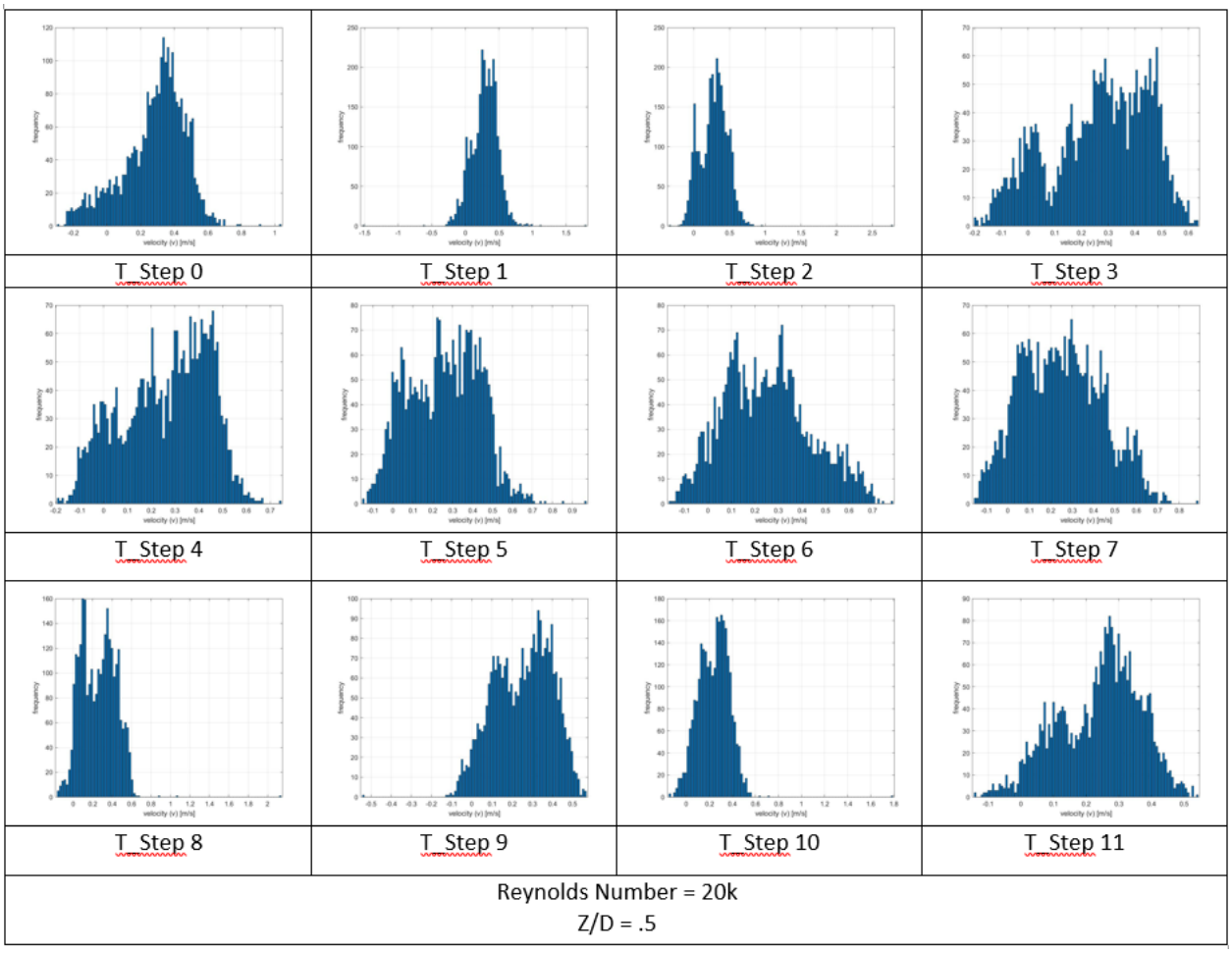

Figure 4.37: Velocity Histogram for Reynolds number 20000 at Z/D = .5

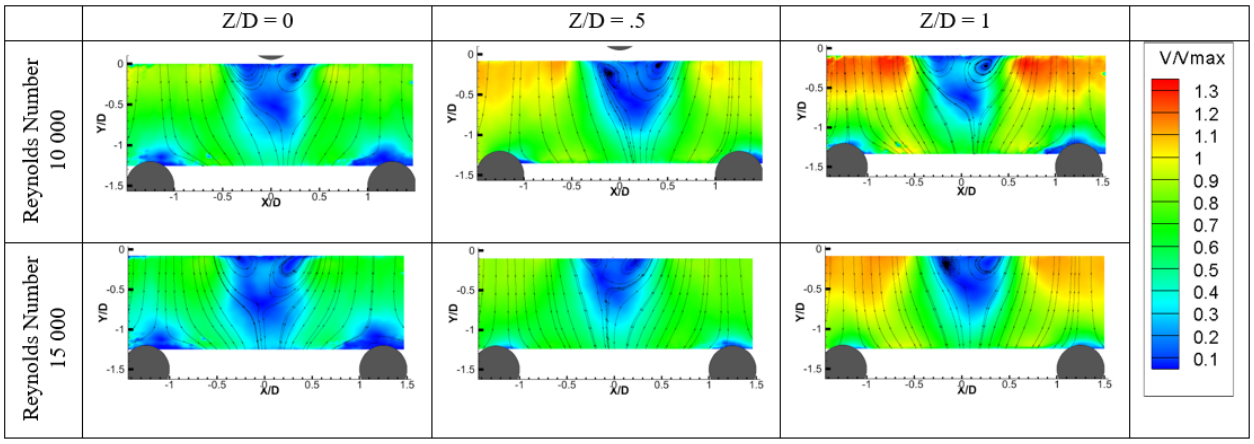

Figure 4.38: Velocity Profiles of Various Z/D and Reynolds number

Finally PIV plots of Q-Criteria are shows in Figure 4.39, the Q-Criteria is plotted as a means to find vortex location as well as relative strength. It is calculated based on the Q-Criteria, found in the following Equation 4.5. Where omega and S are the vorticity and strain rate tensor respectively. Positive values of Q implies that the vorticity is stronger in magnitude compared to the strain rate magnitude.

$$Q = \frac{1}{2} * (\Omega^2 - S^2) \tag{4.5}$$

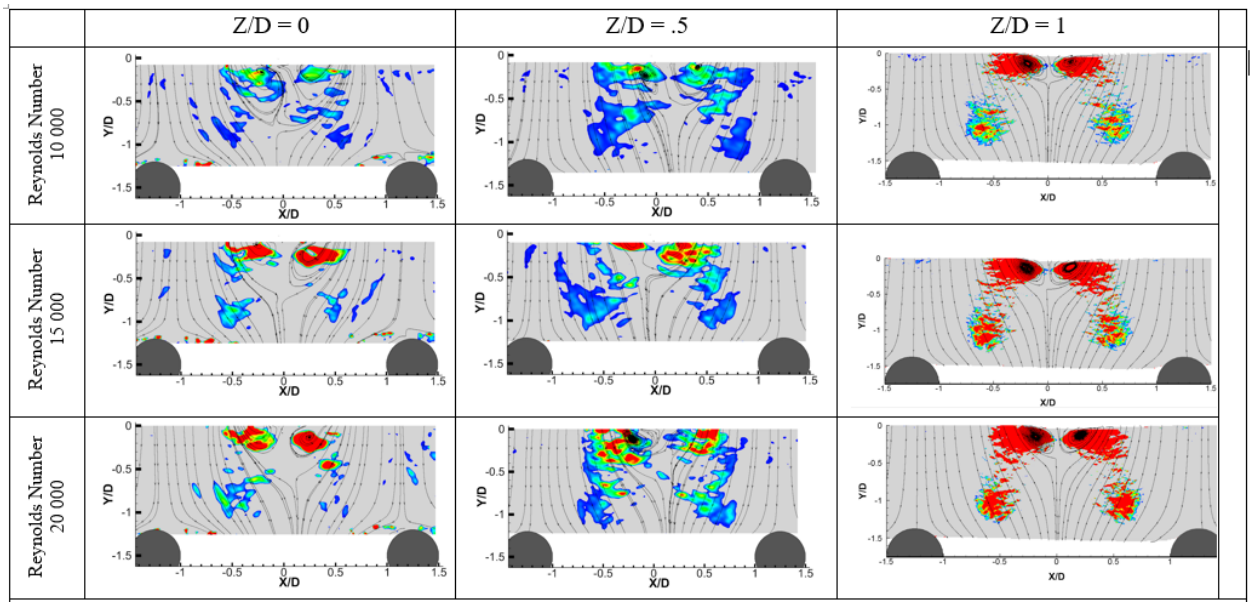

Figure 4.39: Q-Criterian plot from Time Averaged data

Q-Citerian was calculated on the flow field. This method will find Z-plane vortex structures that are dominate by a subtracting the relative strength of vorticity and shear rate. Positive values are plotted, and all negative values are ignored. Although HSV systems were previously found and suggested, they would appear only planes of rotation, that is the HSV system forms in the velocity vector direction Z direction, in the direction on the pin height near the end wall. These spatial modes are prominent in the planes integrated, which can also be found by the histogram. It was found that the quarter plane the vortex from the Q-Criterian is more sparsely spaced out compared to that of the mid line. In the mid line there are well defined areas where the re-circulation zone is, as well as the area with symmetry and very out of plane motion. The quarter plane is very subjective to 3D flow fields, which also suggest that the area 3D gradients which was not captured with 2D PIV. The Z/D plane showed few areas where vortex structures where found, however, they were very weak in magnitude. This suggest that the flow is attached wall with the formation of

random eddies being formed by the horseshoe vortex being lifted from the previous row.

CHAPTER 5: CONCLUSION

In this study several Reynolds number and wall normal planes were interrogated by a PIV technique for Z/D = 0, Z/D = .5, and Z/D = 1 and numerically modeled by CFD. The primary focus was to find vortex structures and properties found in the wake region and where unsteady features are formed. Both the PIV and CFD were in good agreement in the bulk flow, however some velocity traces differ in shape in the spatial area with vortices and wake formation are found in the PIV. Fine or small vortex structures are not seen in the time average sense, as they are washed out by the bulk flow or strong circulation zone and vanishes in the ensemble average. Therefore a modal analysis was used as to track the Y component of velocity to find any indication of secondary flow structures at various time steps based increases of 10 % of the shedding frequency found through the power spectral density. The modal analysis performed by the means of histograms of V velocities at given time step are the only indicator of time resolved PIV measurements. It was also found that the a few histogram were purely Gaussian in distribution, suggesting that no vortex structure was found and the flow field is dominated by the bulk flow. The pure Gaussian was only found at Z/D of 0, and at Reynolds number of 10,000. The Z/D of .5 and Z/D =1 always showed a histogram which showed distinct bulk flow, as well as up to four dominate vortex modes. Therefore, it is believed that the mid line is highly effected by the wake shedding, the quarter plane is affected by HSV as well as wake shedding, and limited vortex structures penetrate the region in the near wall region at lower Reynolds number. For the cases that a Gaussian occurred, it suggest that the Z/D =0 plane, the flow field is mostly attached to the wall and is in the near or in the viscous sub layer with a weak influence of vorticity compared to Z/D of .5 and Z/D = 1.

It was found that terms of mean or bulk flow field, the velocity field seems to match with what is found in literature as well as the CFD study that was performed. As the Reynolds number increase, the re circulation zone length decrease, and the vortex shedding length increases. It was also found that the vortex shedding with decreases as Z/D away from the mid plane. As determined

in the experimental results, the constant motion of the renewed vortices, such as the wake and VK vortices causes the time-averaged flow to appear smeared out. However, it should be noted that the wake region is not attenuated, that is both left and right vortex pairs do not occur at the same time as it might look in time averaged plot. For this reason, only very coherent vortex, such as primary wake can be found using averaged results which is compared to steady numerical models models.

It was found that a CFD model with steady RANS was not able to predict vortex shedding, while URANS was able to do was with some accuracy. RANS models were able to correctly find mean flow field, as well as the vortex shedding length. This suggest there is still a large gap in turbulence and vortex modeling that can be improved by numerical studies.The author suggest that more computationally heavy simulations to be used, such as DES or DNS, to model these vortex structures. Other parameters that were quantified by PIV and not used in this study could be used in validating numerical models, which is planned in the future work. It is also suggested that other dominate area such as the HSV system be studied as well, or the region between the pins in spanwise direction.

APPENDIX A: RIG PICTURES

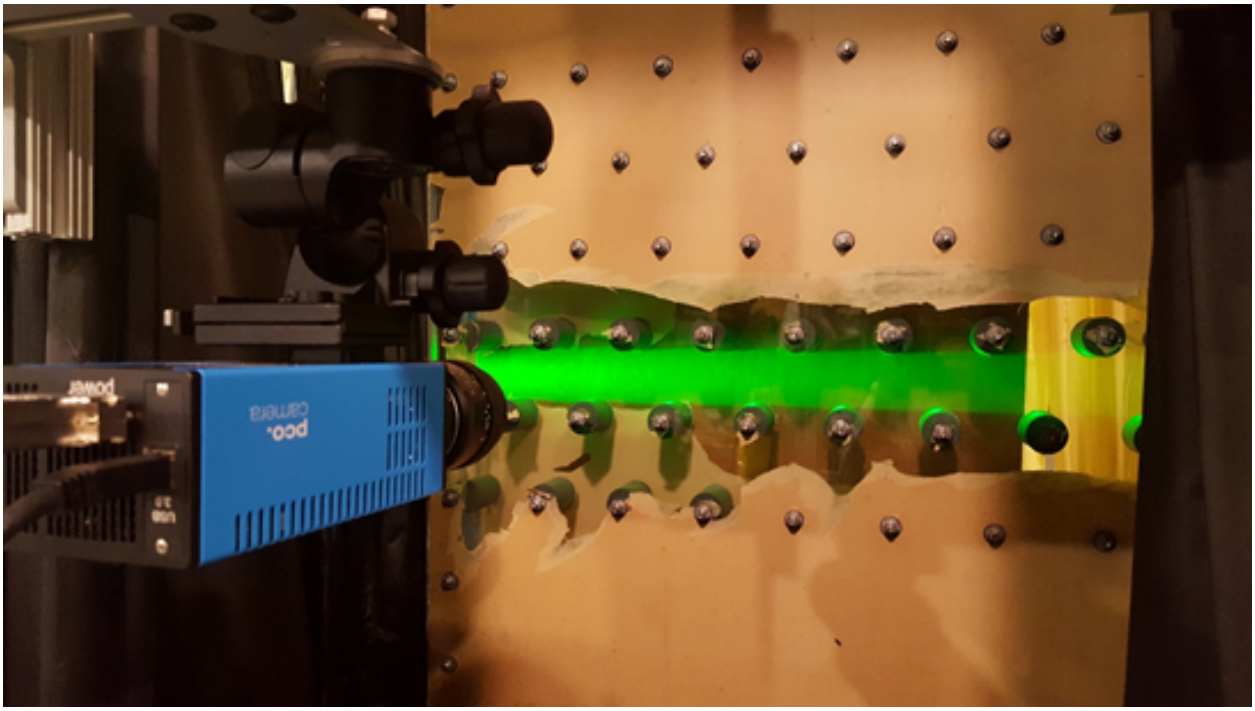

Figure A.1: Laser Sheet of Test Setup

Figure A.2: Tank of Test Setup

Figure A.3: Water Pump and Filter System of Test Setup

APPENDIX B: MATLAB CODE

```
clear
clc

NI6215 = daq.createSession('ni');
NI6215.Rate = 20;
NI6215.DurationInSeconds = 60;
addAnalogInputChannel(NI6215,'dev1', 1, 'Voltage');
data.Voltage = NI6215.startForeground;
data.PressurePSI = data.Voltage*2-2;
data.PressureH20 = data.PressurePSI *27.7076;
data.Pressure = mean(data.PressureH20);

VenturiCurve = xlsread('VenturiCalibration.xlsx');
VCF = fit(VenturiCurve(:,1),VenturiCurve(:,2),'power1');
dp = .8491*data.Pressure+.0083; %% Flow correction

Flowrategpm = VCF(dp);
Flowratecms = Flowrategpm * 6.309*10^-5;
Density = 999;
mu = 8.89*10^-4;
Perimeter = 1.62;
Re_dh = 4*Density*Flowratecms/(mu*Perimeter);
Re_p = Re_dh/2.16781436
Vmax = Re_p/43733.49;

plot(data.PressureH20)
```

Figure B.1: Pressure Collection and Flow Measurement

```
clear
clc

vid = videoinput('pcocameraadaptor')
src = getselectedsource(vid);

NumImages = 10;

vid.FramesPerTrigger = 1;
src.E2ExposureTime = 100000;

for i = 1:NumImages
Data(i).Frame = getsnapshot(vid);
end
%%

save(['Camera' '_' datestr(datetime,30) '.mat'],'Data');
```

Figure B.2: Save Single Snapshot from Camera

LIST OF REFERENCES

[1] Spakovszky, Z. S, *Thermodynamics and Propulsion*. Cambridge, MA: MIT Press, 2017.

[2] J.C.Han and H.C.Chen *Turbine Blade Internal Cooling Passages with Rib Turbulators*. Journal of Propulsion Power, 2006.

[3] Ostanek, J. K., and Thole, K. A. *Effect of streamwise spacing on periodic and random unsteadiness in a bundle of short cylinders confined in a channel* Exp. Fluids, 2012

[4] R. D. Blevins *Flow-induced vibration*. Van Nostrand Reinhold Co., Inc, 1990.

[5] J. C. Han, S. Ou, J. Park and C. K. Lei, *Augmented Heat Transfer in Rectangular Channels of Narrow Aspect Ratios with Rib Turbulators*. Journal of Propulsion Power, 1989.

[6] F. P. Berger, K.-F. Hau and F.-L. Hau, *Local Mass/ Heat Transfer Distribution on Surfaces Roughened with Small Sqaure Ribs* International J. Heat and Mass Transfer 1978.

[7] J. Bailey and R. Bunker, *Heat Transfer and Friction in Channels with Very High Blockage 45 Staggered Turbulators* ASME Tubo Expo 2003.

[8] Z. Wang, P. T. Ireland, S. T. Kohler and J. W. Chew, *Heat Transfer Measurements to a Gas Turbine Cooling Passage with Inclined Ribs* Journal of Turbomachinary 1998.

[9] Zukauskas, A, *Heat transfer from tubes in crossflow* Advances in heat transfer 1972.

[10] Baker, C., *The turbulent horseshoe vortex* Journal of Wind Engineering and Industrial Aerodynamics 1980.

[11] VanFossen G.J., *Heat-Transfer Coefficients for Staggered Arrays of Short Pin Fins* Journal of Engineering for Power 1982.

[12] Simoneau, R., and VanFossen, G., *Effect of location in an array on heat transfer to a short cylinder in crossflow* Journal of Heat Transfer 1984.

[13] Brigham, B. A., and VANFOSSEN, G. J., *Length to diameter ratio and row number effects in short pin fin heat transfer* ASME, Transactions, Journal of Engineering for Gas Turbines and Power 1984.

[14] Metzger D.E., Haley S.W., *Heat Transfer Experiments and Flow Visualization for Arrays of Short Pin Fins* ASME Turbo Expo 1982.

[15] Ames F.E., Dvorak L.A., *Turbulent Transport in Pin Fin Arrays – Experimental Data and Predictions* ASME Turbo Expo 2005.

[16] Bianchini C., Facchini B., Simonetti F., Tarchi L., Zecchi S., *Numerical and Experimental Investigation of Turning Flow Effects on Innovative Pin Fin Arrangements for Trailing* ASME Turbo Expo 2012.

[17] Uzol O., Camci C, *Pressure Loss and Flow Field Measurements Downstream of Staggered Two-Row Circular and Elliptical Pin Fin Arrays* Journal of Heat Transfer 2005.

[18] Ostanek, Jason, Thole, Karen., *Wake development in staggered short cylinder arrays within a channel* Experiments in Fluids 2012.

[19] Bunker, Ronald S., *A review of shaped hole turbine film-cooling technology*. Journal of heat transfer, 2005.

[20] B. Wieneke and A. Sciacchitano, *PIV Uncertainty Propagation* 11th International Symposium on Particle Image Velocimetry-PIV15, 2015

[21] Aga, V., Rose, M., Abhari, R.S, *Experimental Flow Structure Investigation of Compound Angled Film Cooling*. ASME Journal of Turbomacheriny, 2008.

[22] Boyce, Meherwan P, *Gas turbine engineering handbook*. Elsevier, 2012.

[23] Aga, V., Rose, M., Abhari, R.S, *A CFD INVESTIGATION ON THE EFFECTS OF ENTRANCE CROSSFLOW DIRECTIONS TO FILM-COOLING HOLES*. American Society of Mechanical Engineers, Heat Transfer Division, 1997.

[24] Irvine, Thomas Francis, *Advances in heat transfer. Vol. 23*. Academic Press, 1993.

[25] J. C. Han, J. S. Park and C. K. Lei, *Heat Transfer and Pressure Drop in Blade Cooling Channels with Turbulence Promoters*. NASA Contractor Report 3837, 1984.

[26] J. C. Han, L. R. Glicksman and W. M. Rohsenow, *An Investigation of Heat Transfer and Friction for RibRoughened Surfaces* International Journal Heat and Mass Transfer, 1978.

[27] S. J. Kline and F. A. McClintock, *Describing Uncertainties in Single Sample Experiments* Mechanical Engineering, vol. 75, no. 1, pp. 3-8, 1953